

CHARACTERIZING ULTRAVIOLET AND INFRARED OBSERVATIONAL PROPERTIES FOR GALAXIES. II. FEATURES OF ATTENUATION LAW

YE-WEI MAO^{1,2,3}, XU KONG^{2,3}, LIN LIN⁴

Draft version April 20, 2021

ABSTRACT

Variations in the attenuation law have a significant impact on observed spectral energy distributions for galaxies. As one important observational property for galaxies at ultraviolet and infrared wavelength bands, the correlation between infrared-to-ultraviolet luminosity ratio and ultraviolet color index (or ultraviolet spectral slope), i.e., the IRX-UV relation (or IRX- β relation), offered a widely used formula for correcting dust attenuation in galaxies, but the usability appears to be in doubt now because of considerable dispersion in this relation found by many studies. In this paper, on the basis of spectral synthesis modeling and spatially resolved measurements of four nearby spiral galaxies, we provide an interpretation of the deviation in the IRX-UV relation with variations in the attenuation law. From both theoretical and observational viewpoints, two components in the attenuation curve, the linear background and the 2175 Angstrom bump, are suggested to be the parameters in addition to the stellar population age (addressed in the first paper of this series) in the IRX-UV function; different features in the attenuation curve are diagnosed for the galaxies in our sample. Nevertheless, it is often difficult to ascertain the attenuation law for galaxies in actual observations. Possible reasons for preventing the successful detection of the parameters in the attenuation curve are also discussed in this paper, including the degeneracy of the linear background and the 2175 Angstrom bump in observational channels, the requirement for young and dust-rich systems to study, and the difficulty in accurate estimates of dust attenuations at different wavelength bands.

Subject headings: dust, extinction - galaxies: ISM - galaxies: spiral - infrared: galaxies - ultraviolet: galaxies

1. INTRODUCTION

The relation between the ratio of infrared (IR) to ultraviolet (UV) luminosities (i.e., IR excess, or IRX) and the ultraviolet spectral slope (β) initially found in starburst galaxies by Meurer et al. (1999, i.e., the IRX- β or IRX-UV relation) offers a prescription for correcting internal dust attenuation for galaxies. This empirical formula has been in particular applied to high redshift galaxies from which the rest-frame UV emission can be observed by ground-based optical telescopes (e.g., Daddi et al. 2004, 2007; Kong et al. 2006; Martin et al. 2007; Bouwens et al. 2009). However, the considerable deviation in the IRX-UV relation encountered in studies of normal galaxies on either an integrated or spatially resolved basis casts doubt on the utility of this attenuation diagnostics (e.g., Bell 2002; Kong et al. 2004; Buat et al. 2005; Seibert et al. 2005; Johnson et al. 2007; Boquien et al. 2009). Differences in the stellar population have been assumed to be a pivotal driver of the deviation in the correlation between IRX and β (Kong et al. 2004; Muñoz-Mateos et al. 2009). However, a number of statistical studies of galaxies adopted relevant spectral indices to trace different stellar populations and did not found any solid trend of the IRX-UV relation with stellar populations (e.g., Seibert et al. 2005; Johnson et al. 2007; Boquien et al. 2009). At the same time, radiative transfer simulations have provided additional insight into the disparities of spectral energy distributions (SEDs) for galaxies

with diverse attenuation/extinction properties (Witt & Gordon 2000; Calzetti 2001; Inoue et al. 2006). As a result, variations in attenuation/extinction law have been considered to be an additional interpretation of the observed dispersion in the IRX-UV relation (Burgarella et al. 2005; Panuzzo et al. 2007; Boquien et al. 2012).

The terminology "*attenuation*" describes the margin between the intrinsic and observed radiation magnitudes, ascribed to all complex effects of the dust opacity on incident emission, including absorption and scattering by dust grains with the geometric configuration between dust and stars taken into account; as an idealized approximation, homogeneous dust screens in the foreground of stars are often assumed to handle actual observations, and this kind of dust effect is defined as "*extinction*" which correlates only with the optical depth of the dust medium (see Calzetti 2001, for more thorough discussion about the terminologies).

Observations of pointlike sources such as individual stars inside galaxies are used to study extinction law. Through a spectral inspection of a set of individual reddened stars from different sightlines inside our Milky Way (MW), Fitzpatrick & Massa (1988, 1990, hereafter denoted as FM) have obtained a parameterized description of dust extinction as a function of wavelength, formulated in terms of five coefficients as follows:

$$\frac{A(\lambda)}{E(B-V)} = c_1 + c_2 \lambda^{-1} + c_3 \frac{\lambda^{-2}}{(\lambda^{-2} - \lambda_0^{-2})^2 + \gamma \lambda^{-2}} + c_4 F(\lambda^{-1}) + R_V, \quad (1)$$

where

$$F(\lambda^{-1}) = \begin{cases} 0.5392(\lambda^{-1} - 5.9)^2 + 0.0564(\lambda^{-1} - 5.9)^3, & \text{for } \lambda^{-1} \geq 5.9 \mu\text{m}^{-1}, \\ 0, & \text{for } \lambda^{-1} < 5.9 \mu\text{m}^{-1}. \end{cases} \quad (2)$$

¹ Purple Mountain Observatory, Chinese Academy of Sciences, Nanjing 210008, China; ywmao@pmo.ac.cn

² Center for Astrophysics, University of Science and Technology of China, Hefei 230026, China; xkong@ustc.edu.cn

³ Key Laboratory for Research in Galaxies and Cosmology, USTC, CAS, Hefei 230026, China

⁴ Shanghai Astronomical Observatory, Chinese Academy of Sciences, Shanghai 200030, China; linlin@shao.ac.cn

The wavelength λ is the free variable in units of μm . Equation (1) characterizes an extinction curve with three components: a linear background component ($c_1 + c_2\lambda^{-1}$), a bump component ($c_3\lambda^{-2}/((\lambda^{-2} - \lambda_0^{-2})^2 + \gamma\lambda^{-2})$), and a far-UV (FUV) rise component ($c_4F(\lambda^{-1})$). The bump component in the extinction curve was initially detected by Stecher (1965) and is constantly centered at the wavelength of 2175 Angstrom (i.e., $\lambda_0^{-1} = 4.596 \mu\text{m}^{-1}$). The mean values of the five coefficients for MW have been found to be $c_1 = 2.030 - 3.007c_2$, $c_2 = 0.698$, $c_3 = 3.230$, $c_4 = 0.410$ and $\gamma = 0.990$ (Fitzpatrick 1999). A prominent 2175 Angstrom bump is the most appealing property in the MW extinction curve. In Equation (1), $R_V (\equiv A(V)/E(B-V))$ is the ratio of total to selective extinction, and $R_V = 3.1$ is the best fit for MW. By adjusting the coefficients, the FM parameterization is able to produce a variety of extinction curves with different properties of the three components. At present, the FM formula has been successfully applied not only to our Galaxy but also to our neighbors, including the Magellanic Clouds (Gordon et al. 2003). In contrast to our Galaxy, the Small Magellanic Cloud (SMC) presents a lack of a 2175 Angstrom bump and a much steeper linear background in the extinction curve (see Gordon et al. 2003, for more details).

An alternative form of the extinction curve has been provided by Cardelli et al. (1989, hereafter denoted as CCM) with a similar study of individual stars from different sightlines in the MW, parameterized only with the total-to-selective extinction R_V :

$$\frac{A(\lambda)}{E(B-V)} = R_V \cdot a(\lambda) + b(\lambda), \quad (3)$$

where $a(\lambda)$ and $b(\lambda)$ are piecewise functions of λ in different wavelength ranges (see Cardelli et al. 1989, for more details). O'Donnell (1994) has updated this R_V -dependent extinction law at optical and near IR wavelength bands. In the UV range ($\lambda^{-1} \geq 3.3 \mu\text{m}^{-1}$, or $\lambda \leq 3030$ Angstrom), the CCM description is in agreement with the FM parameterization for the MW mean values when $R_V \sim 3.1$. However, convincing evidence of this R_V -dependent law has not been found for other galaxies, e.g., the Magellanic Clouds (Clayton et al. 1996; Gordon et al. 2003; Cartledge et al. 2005), M31 (Hutchings et al. 1992; Bianchi et al. 1996), and M101 (Rosa & Benvenuti 1994).

Different from spatially resolved pointlike sources, in the case of galaxies as a whole, dust mediums are mixed with stars rather than emerging as foreground screens, and the dust obscuration therefore becomes dust attenuation. Calzetti et al. (2000, hereafter denoted as C00) have investigated a sample of local starburst galaxies through integrated measurements and derived an empirical formula of the attenuation curve from polynomial fitting to characterize the complex effects of dust obscuration. This curve, distinct from those found in the MW and our neighbors, shows a smooth shape and moderate slope without any bump feature. A power-law form of the curve with $\lambda^{-0.7}$ has been suggested to suitably reproduce the C00 polynomial expression for starburst galaxies (Charlot & Fall 2000). The featureless shape of the C00 attenuation curves is generally believed to be an aftermath of the statistical approximation and in particular of the "age-selective attenuation" which describes a trend of increasing attenuation for younger stellar populations prevalent in integrated measurements of galaxies (Granato et al.

2000; Panuzzo et al. 2007). Notwithstanding, the exact form of the attenuation curve for normal galaxies is still unclear. Recent studies have revealed extensive variations in both of the slope and the 2175 Angstrom bump between different galaxies at either low or high redshift (e.g., Noll et al. 2007, 2009; Conroy et al. 2010; Jiang et al. 2011; Wild et al. 2011; Buat et al. 2011, 2012).

In the first paper of this series (Mao et al. 2012, hereafter denoted as Paper I), we have carried out a spatially resolved study of galaxies, focusing on effects of stellar population age on the IRX-UV relation. In that work, we have divided the measured subregions inside each galaxy into UV clusters representing young stellar populations and diffuse regions in galactic background representing evolved stellar populations. The age effects appear as systematic offset of the local background regions toward redder colors from the UV clusters in the IRX-UV diagrams; at the same time, complexities in the star formation history (SFH) are suggested to disperse the age effects, and therefore interpret the different levels of overlapping between the UV clusters and the local background regions in the IRX-UV diagrams. However, in Paper I, we assume the C00 attenuation law in the scenarios with dust attenuation and stellar population age addressed as two parameters for interpretation of the observational data. On the basis of this assumption, a few results present a discrepancy between observations and modeling which raises a realistic requirement for more parameters in the IRX-UV function.

As a follow-up of the work in Paper I, in this paper we concentrate on features of the attenuation law in an attempt to find other potential parameters in the IRX-UV function, and we offer a complementary explanation of the observational data. Throughout the paper, consistent with Paper I, IRX is defined as the IR-to-FUV luminosity ratio in the form of a logarithm, $\text{IRX} \equiv \log(L(\text{IR})/L(\text{FUV}))$, where $L(\text{IR})$ is total IR luminosity radiated by dust in the wavelength range of 3–1100 μm , and $L(\text{FUV}) = \nu L_\nu(\text{FUV})$ is the FUV luminosity of stellar emission. The UV color is defined as $\text{FUV} - \text{NUV}$, where the FUV and NUV wavebands correspond to the FUV and NUV channels of the *Galaxy Evolution Explorer* (GALEX; $\lambda_{\text{eff}}(\text{FUV}) = 1516$ Angstrom and $\lambda_{\text{eff}}(\text{NUV}) = 2267$ Angstrom; Bianchi et al. 2003; Martin et al. 2005).

The remainder of this paper is organized as follows. In Section 2, we predict impacts of attenuation curve on the IRX-UV relation on the basis of modeling. In Section 3, we provide an observational insight into the predicted features of the attenuation curve through a spatially resolved study of nearby galaxies. In Section 4, by employing an artificial sample, we assess the reliability of the characterization in previous sections and provide a prescription for quantitative constraints on the attenuation curve. In Section 5, we discuss the main difficulties that potentially prevent a successful detection of the features of the attenuation law in actual observations. Finally, we summarize the results and have a brief outlook on the nature of variations in attenuation law in Section 6.

2. PREDICTION FROM MODELING

In this section, we carry out a theoretical inspection of possible diversification in the IRX-UV function related to variations in the attenuation curve on the basis of modeling with a combination of stellar population synthesis and attenuation curves. We obtain stellar population SEDs with a series of ages from the STARBURST99 spectral synthesis library (Leitherer et al. 1999; Vázquez & Leitherer 2005), assuming an instantaneous burst, constant metallicity of $Z = 0.02$ and

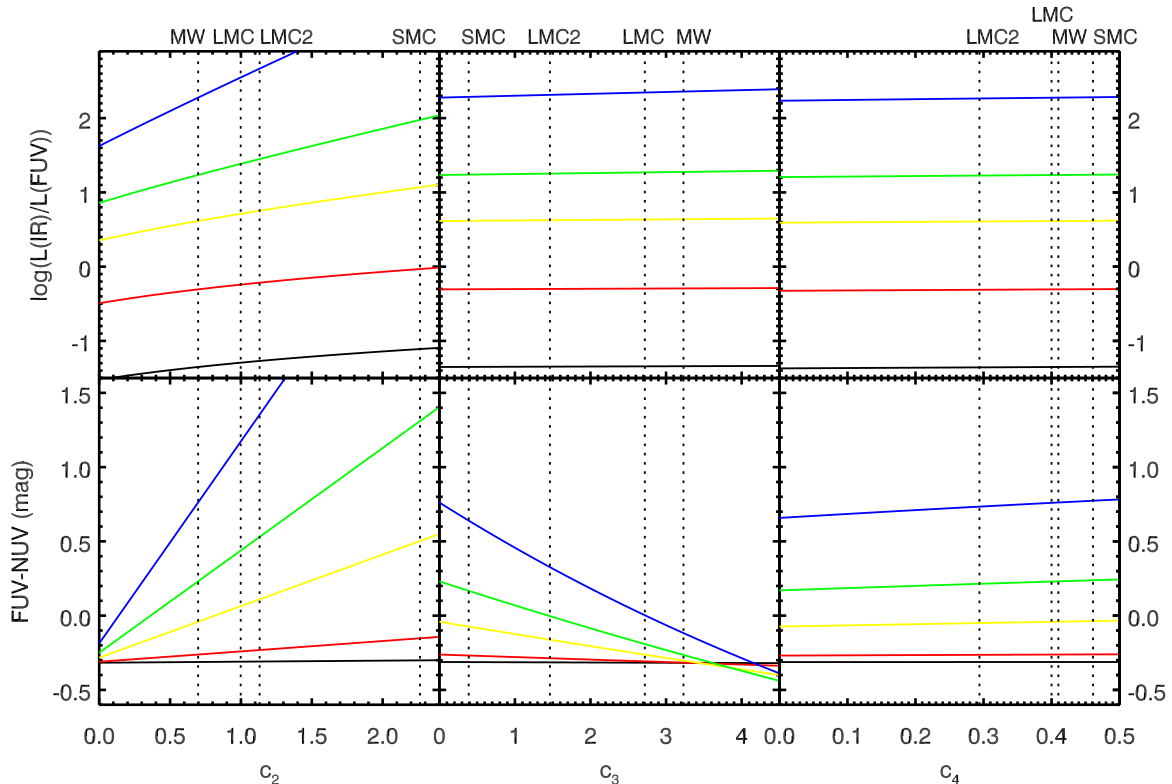


Figure 1. IRX (top row) and FUV–NUV (bottom row) vs. c_2 (left column), c_3 (middle column), and c_4 (right column) coefficients in the FM formula. The solid lines in each panel show the modeled correlations at five fixed amounts of dust attenuation: $A(V) = 0.01$ (black), 0.1 (red), 0.5 (yellow), 1.0 (green), and 2.0 (blue) mag; the dotted lines give an example of special fits for the MW, the LMC, the LMC2, and the SMC attenuation curves.

the Kroupa (2002) initial mass function with exponents of 1.3 over $0.1\text{--}0.5 M_{\odot}$ and 2.3 over $0.5\text{--}100 M_{\odot}$.

Although what we study is attenuation rather than extinction, the FM parameterization (Equation (1)) is employed to construct the attenuation curves in our work. The FM formula is formulated from observations of individual stars in our Galaxy, where the geometric configuration can be simply described by a homogeneous dust screen in the foreground of stars (attenuation in this case is defined as extinction), whereas in the case of galaxies as a whole, or subregions inside galaxies where individual stars cannot be resolved, actual geometries are more complex than the foreground screen. Nevertheless, the geometrical effects only exert influences on the existing parameters in the attenuation curve such as the linear background slope and the 2175 Angstrom bump strength, and are unlikely to add new parameters. In this situation, the FM formula is valid to reproduce attenuation curves that have been affected by different geometries. We will present a simple test for verifying the validity of the FM parameterization in the case of various dust-star geometries in Appendix A.

The attenuated spectra in modeling are convolved with transmission curves of the *GALEX* FUV and NUV filters to obtain modeled FUV and NUV magnitudes. The IR luminosity is estimated on the principle of the energy balance between attenuated stellar emission and re-emitted thermal radiation by interstellar dust mediums. In this case, the luminosity difference between the intrinsic and attenuated stellar SEDs can be converted to IR luminosity.

The FM analytical formula parameterizes the three compo-

nents in the attenuation curve with five coefficients (c_1 , c_2 , c_3 , c_4 , and γ), as presented in Equation (1), which enables a thorough inspection of each component by adjusting the relevant parameters. In this work, we begin with an examination aimed at inspecting the influence of each single component on IRX and FUV–NUV, respectively. The *GALEX* NUV bandwidth (1771–2831 Angstrom; Morrissey et al. 2007) covers the full range of observed widths of the 2175 Angstrom bump (FWHM $\sim 360\text{--}600$ Angstrom; Fitzpatrick & Massa 1986), and in this case, the bump area ($A_{\text{bump}} \equiv \pi c_3 / (2\gamma)$; Fitzpatrick & Massa 1986, 2007) becomes the only factor responsible for the impact of the bump on broadband photometric results. Therefore, we fix the width of the 2175 Angstrom bump (γ) to the MW mean value ($\gamma = 0.99 \mu\text{m}^{-1}$) in this inspection, and then the bump area is solely determined by the coefficient c_3 . By taking the coefficient c_1 in linear correlation with c_2 into account (Fitzpatrick 1999), the final variable parameters are c_2 (linear background slope), c_3 (2175 Angstrom bump strength), and c_4 (FUV rise curvature), and we define the values $c_2 = 0.698$, $c_3 = 0.0$, and $c_4 = 0.410$ (i.e., the MW mean values for the linear background slope and the FUV curvature, but no bump) as a standard reference. During the procedure, we vary one coefficient and fix the other two to this reference at each time. This approach allows us to individually inspect the three coefficients, c_2 , c_3 , and c_4 .

The modeling results are plotted in Figure 1 which shows IRX and FUV–NUV as a function of the coefficients c_2 , c_3 , and c_4 separately, for five constant amounts of dust attenuation ($A(V) = 0.01$, 0.1, 0.5, 1.0, and 2.0 mag). Four typical values for the coefficients, i.e., the MW, the SMC, the Large

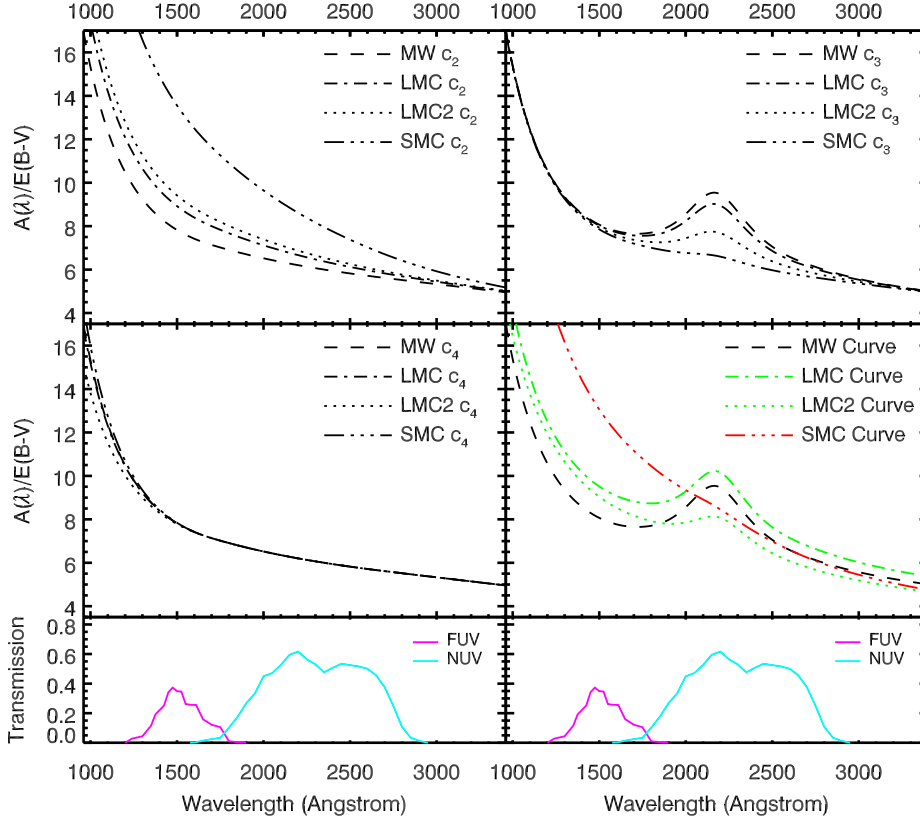


Figure 2. Attenuation curves created with Equation (1) at the UV wavelength range. The top left panel shows the curves with different c_2 : the MW c_2 (black dashed line), the LMC c_2 (dot-dashed line), the LMC2 c_2 (dotted line), and the SMC c_2 (triple-dot-dashed line), with $c_3 = 0.0$ and other coefficients fixed to the MW values. The top right panel shows the curves with different c_3 : the MW c_3 (black dashed line), the LMC c_3 (dot-dashed line), the LMC2 c_3 (dotted line), and the SMC c_3 (triple-dot-dashed line), with other coefficients fixed to the MW values. The middle left panel shows the curves with different c_4 : the MW c_4 (black dashed line), the LMC c_4 (dot-dashed line), the LMC2 c_4 (dotted line), and the SMC c_4 (triple-dot-dashed line), with $c_3 = 0.0$ and other coefficients fixed to the MW values. The middle right panel shows the MW curve (dashed line), the LMC curve (dot-dashed line), the LMC2 curve (dotted line), and the SMC curve (triple-dot-dashed line) curves. Filter transmission curves of the *GALEX* FUV (magenta) and NUV (cyan) bands are shown in the bottom panels.

Magellanic Cloud (LMC), and the supershell area of the Large Magellanic Cloud (LMC2), are marked in each panel of Figure 1, where the MW values are obtained from Fitzpatrick (1999), and the LMC, LMC2, and SMC values are obtained from Gordon et al. (2003). In this figure, FUV–NUV is in positive correlation with c_2 , and in negative correlation with c_3 ; the amplitude of the variations in FUV–NUV tends to increase at heavier attenuation. For instance, in the bottom left panel of Figure 1, a variation of c_2 from 0.698 (the MW value) to 2.264 (the SMC value) reddens FUV–NUV by a factor of ~ 0.6 mag at $A(V) = 0.5$ mag and ~ 1.1 mag at $A(V) = 1.0$ mag; in the bottom middle panel, a variation of c_3 from 0.389 (the SMC value) to 3.230 (the MW value) diminishes the reddening in FUV–NUV by a factor of ~ 0.2 mag at $A(V) = 0.5$ mag and ~ 0.4 mag at $A(V) = 1.0$ mag. IRX is in positive correlation with c_2 , and keeps constant with variations in c_3 . In contrast to c_2 and c_3 , the coefficient c_4 has no effective impact on either IRX or FUV–NUV.

Figure 2 shows the attenuation curves with c_2 , c_3 , and c_4 varying at one time, respectively, in the top left, top right, and middle left panels, corresponding to the left, middle, and right columns of Figure 1. The MW, LMC, LMC2, and SMC values of the three coefficients are employed to actualize the variations. Consistent with the approach for Figure 1, a single coefficient varies, and the others are set to the standard reference at the same time. In the middle right panel of Figure 2, the intact MW, LMC, LMC2, and SMC curves are dis-

played. This exhibition offers more intuitive views of the different properties in the attenuation curve at the FUV and NUV bands. As can be seen, the slope of the linear background preferentially affects the FUV band (1344–1786 Angstrom), while the 2175 Angstrom bump dominates in the NUV wavelength range (1771–1831 Angstrom). The separate effects of the linear background and the 2175 Angstrom bump on FUV and NUV attenuations in turn clarify the different trends of FUV–NUV with c_2 and c_3 in Figure 1. This inspection expects the linear background and the 2175 Angstrom bump in the attenuation curve to have conspicuous impacts on IRX and FUV–NUV, and consequently we will focus on the two components in the following investigations.

In order to better trace the performance of the linear background and the bump in the IRX–UV function, we construct two more attenuation curves: one with the MW-type slope ($c_2 = 0.698$) and the SMC-type bump ($c_3 = 0.389$), and the other with the SMC-type slope ($c_2 = 2.264$) and the MW-type bump ($c_3 = 3.230$). Combining the two artificial curves with the MW and SMC curves, we have four attenuation curves with different combinations of the two parameters c_2 and c_3 as a template: the MW curve (representing a shallow slope and a prominent bump),⁵ the curve with the MW c_2 and the SMC

⁵ Hereafter, we use the "MW curve" to denote the attenuation curve with the MW-type parameters, which could be affected by dust-star geometries and are therefore conceptually different from the MW extinction curve. In

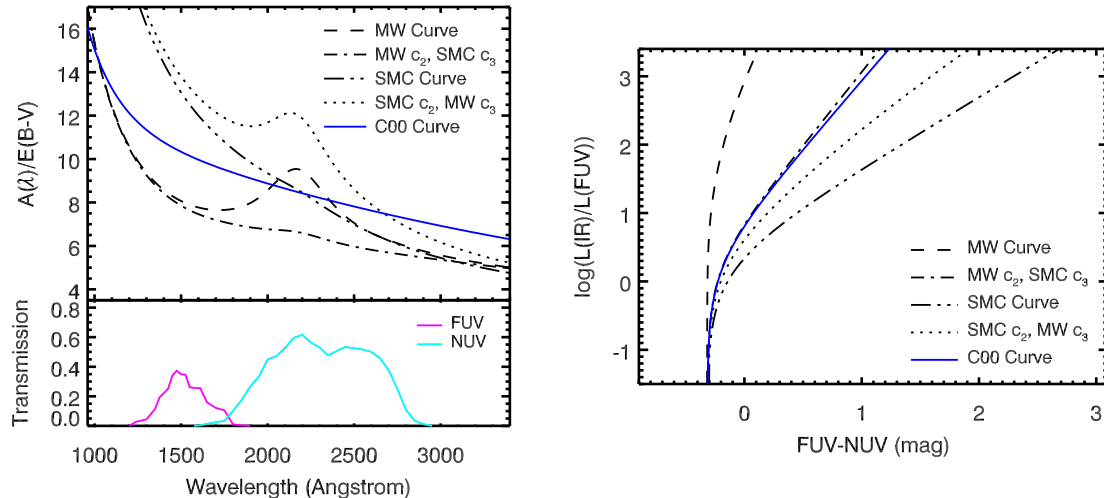


Figure 3. Left: attenuation curves with different combinations of c_2 and c_3 at UV wavelength range, including the MW curve (black dashed line), the M-S curve (black dot-dashed line), the SMC curve (black triple-dot-dashed line), the S-M curve (black dotted line), and the C00 curves (blue solid line); filter transmission curves of the *GALEX* FUV (magenta) and NUV (cyan) bands are also shown. Right: IRX-UV tracks reproduced with the attenuation curves shown in the left panel.

c_3 (hereafter denoted as the M-S curve, representing a shallow slope and a trivial bump), the SMC curve (representing a steep slope and a trivial bump), and the curve with the SMC c_2 and the MW c_3 (hereafter denoted as the S-M curve, representing a steep slope and a prominent bump). The four attenuation curves are displayed in the left panel of Figure 3, with the C00 curve superimposed for comparison purposes. It is apparent to see that the C00 curve is comparable with the MW curve in slope within the wavelength range of > 1500 Angstrom, albeit with an offset due to the larger value of the total-to-selective extinction for the C00 curve ($R_V = 4.05$ for the C00 curve, while in the modeling we adopt $R_V = 3.1$).

The right panel of Figure 3 shows the IRX-UV tracks reproduced with the four template attenuation curves and the C00 curve as displayed in the left panel of this figure. In this diagram, all the tracks span a range from -1.5 to 3.4 in IRX but extend by various orders of magnitude in FUV-NUV. For instance, FUV-NUV varies by ~ 0.4 mag for the MW curve, ~ 1.4 mag for the M-S curve, and ~ 3.0 mag for the SMC curve. The different extents in FUV-NUV on the same IRX scale reflect the distinct features of the linear background and the 2175 Angstrom bump in the IRX-UV function: at constant IRX, the steeper linear background gives rise to redder FUV-NUV, whereas the presence of the 2175 Angstrom bump tends to restrain the reddening effect. As a consequence, with the bump strength decreasing or the linear background steepening, the IRX-UV relation appears to incline toward the redder color space. Such impacts become of more significance at higher IRX levels (i.e., heavier attenuation). For example, the difference in FUV-NUV between the tracks reproduced by the MW curve and the SMC curve ranges from less than 0.2 mag at IRX = 0.0, to about 0.8 mag at IRX = 1.0 and to even over 1.6 mag at IRX = 2.0. It is also worth seeing that in this diagram, the M-S curve and the C00 curve yield consistent IRX-UV tracks, which is ascribed to the similar linear slopes and the same bumpless shape between the M-S curve and the C00 curve (as depicted in the left panel of Figure 3).

the same way, the "SMC curve" described in the text denotes the attenuation curve with the SMC-type parameters.

It should be noted that in the previous inspection, we vary a single parameter and fix the others at each time. This approach is a simplification in order to illuminate the respective role of each parameter. However, it is suggested that the linear background slope probably depends on size distribution of overall dust grains (Weingartner & Draine 2001; Clayton et al. 2003), while the 2175 Angstrom bump could be carried by carbonaceous molecular particles (Chhowalla et al. 2003). Although the carbonaceous molecular particles are usually considered to be small grains, there is a lack of conclusive evidence of the link between the grain size distribution and the grain species distribution. Thus, at present we cannot exclude the possibility that the two components in the attenuation curve are likely to change simultaneously and independently in different environments and as a result have composite effects on FUV-NUV. In the right panel of Figure 3, the IRX-UV track reproduced by the S-M curve is displayed as an example of this degeneracy. Since the presence of the 2175 Angstrom bump decreases the reddening of FUV-NUV, the track presents bluer FUV-NUV than the product of the SMC curve at constant IRX and therefore cannot be easily distinguished from a shallower attenuation curve with a stronger bump. This degeneracy implies a possible complicacy in the detection of attenuation curve features. In Section 4, we will analyze this degeneracy more thoroughly through an investigation with an artificial sample.

3. INSIGHT FROM OBSERVATIONS

The linear background and the 2175 Angstrom bump in the attenuation curve have been expected to be two important operators in the IRX-UV function in the above section by modeling. In this section, we will examine the IRX-UV relation from an observational standpoint and attempt to find observable phenomena linked to the two parameters in the attenuation curve through a spatially resolved study of four nearby galaxies.

3.1. Data

3.1.1. Sample of Galaxies

Table 1
Basic Properties of the Galaxies

Name	R.A. ^a (J2000.0)	Dec. ^a (J2000.0)	Morphology ^a	D_{25} ^a (arcmin)	P.A. ^b (degree)	Distance ^b (Mpc)	M_{Opt} ^a (mag)	$E(B-V)_{\text{GAL}}$ ^{b,c} (mag)	SFR ^a ($M_{\odot} \text{ yr}^{-1}$)
NGC 3031 (M81)	09 55 33.2	+69 03 55	SAab	26.9×14.1	157	3.7	-21.2	0.080	1.1
NGC 4536	12 34 27.0	+02 11 17	SABbc	7.6×3.2	130	15.0	-20.8	0.018	3.7
NGC 5194 (M51a)	13 29 52.7	+47 11 43	SABbc	11.2×6.9	163	7.7	-21.4	0.035	5.4
NGC 7331	22 37 04.1	+34 24 56	SAB	10.5×3.7	171	14.7	-21.8	0.091	4.2

^a Data obtained from Kennicutt et al. (2003).

^b Data obtained from the NASA/IPAC Extragalactic Database.

^c Data obtained from Schlegel et al. (1998).

In Paper I, we compiled five nearby spiral galaxies from the SINGS (Kennicutt et al. 2003) sample and discovered influences of stellar population age on the IRX-UV relation. Nevertheless, in that work some observational data lie out of the interpretation with the adopted SFH scenarios that address stellar population age as the second parameter in the IRX-UV function. In this paper, we select four galaxies in Paper I, NGC 3031, NGC 4536, NGC 5194, and NGC 7331, to further investigate the nature of the IRX-UV relation from the alternative viewpoint of attenuation law.⁶ The basic properties of the four galaxies are presented in Table 1.

3.1.2. Multiwavelength Imaging

Broadband FUV and NUV imaging data were obtained from *GALEX* observations and downloaded from the Multi-mission Archive at Space Telescope Science Institute (MAST) Web site;⁷ $8 \mu\text{m}$ (dust-only⁸) and $24 \mu\text{m}$ images were observed by the *Spitzer Space Telescope* (*Spitzer*, Werner et al. 2004) and retrieved from the SINGS data distribution service.⁹ The original pixel scales are $\sim 1''.5$ for FUV and NUV, $0''.75$ for $8 \mu\text{m}$, and $\sim 1''.5$ for $24 \mu\text{m}$ images. The full widths at half maximum (FWHMs) of point spread function (PSF) for these images are $\sim 5''$ for FUV and NUV, $\sim 2''$ for $8 \mu\text{m}$, and $\sim 6''$ for $24 \mu\text{m}$ images.

$H\alpha$ narrowband imaging data are also employed in this work. The $H\alpha$ narrowband image for NGC 3031 was observed by the 60/90 cm Schmidt telescope at Xing-Long station of the National Astronomical Observatories of China with the filter of transmission profile FWHM ~ 120 Angstrom (Lin et al. 2003). The stellar continuum of the $H\alpha$ image was generated through interpolation between two adjacent intermediate-band imaging data centered at 6075 Angstrom and 7050 Angstrom (which were taken with the same telescope for this galaxies) and subtracted from the $H\alpha$ image. The continuum subtraction and flux calibration for the NGC 3031 $H\alpha$ imaging data are presented in Lin et al. (2003). The $H\alpha$ narrowband images for NGC 4536, NGC 5194, and NGC 7331 were observed by the 2.1 m telescope at Kitt Peak National Observatory with the filter of transmission profile FWHM ~ 67 Angstrom and downloaded from the SINGS data distribution service. For each of the three galaxies,

⁶ There are five galaxies studied in Paper I, whereas in this paper NGC 6946 is not selected since the *GALEX* images for this galaxy are quite noisy, and the data points from this galaxy spread with considerable scatter in the IRX-UV diagram as shown in Paper I, which is inappropriate for the current work.

⁷ <http://galex.stsci.edu/>

⁸ The $8 \mu\text{m}$ data have been transformed into dust-only emission by removing stellar contribution, where the $3.6 \mu\text{m}$ data are adopted as the reference of stellar emission with the scale factor of 0.37 provided in Thilker et al. (2007).

⁹ <http://irsa.ipac.caltech.edu/data/SPITZER/SINGS/>

Table 2
Total Exposure Time of the Imaging Observations
(in units of second)

Name	FUV	NUV	$H\alpha$	$8 \mu\text{m}$	$24 \mu\text{m}$
NGC 3031	14707	29422	37200	6432	220
NGC 4536	1280	1762	900	1286	147
NGC 5194	10787	10787	900	2894	147
NGC 7331	7658	12237	600	1501	147

the stellar continuum of these $H\alpha$ images was produced via rescaling the R band image taken from the same survey, and subtracted from the $H\alpha$ image. Detailed descriptions of the continuum subtraction and flux calibration for these $H\alpha$ images are presented in Kennicutt et al. (2008). The original pixel scales of the $H\alpha$ images are $\sim 1''.7$ for NGC 3031, and $\sim 0''.3$ for NGC 4536, NGC 5194, and NGC 7331. The PSF FWHMs of the $H\alpha$ images are $\sim 4''.9$ for NGC 3031, and about $1''.4$ – $1''.8$ for NGC 4536, NGC 5194, and NGC 7331.

The exposure time for all the imaging observations is listed in Table 2.

3.1.3. Image Processing

The global background is subtracted from the FUV, NUV, and $H\alpha$ images. During this procedure, we mask the galaxy and bright sources in each of the original images and then adopt polynomial fitting along two dimensions in the source-masked images to obtain the global background (see Zheng et al. 1999; Kong et al. 2000; Zou et al. 2011; Lin et al. 2013, for the description of global background subtraction in detail). The global background for the $8 \mu\text{m}$ and $24 \mu\text{m}$ images had already been subtracted before they were released on the Web site.

The PSFs of the FUV, NUV, $H\alpha$, and $8 \mu\text{m}$ images are translated to match that of the $24 \mu\text{m}$ image via convolution of the images with the relevant kernels offered in Aniano et al. (2011). With regard to the ground-based observations, we apply the "Gauss 5.0 to $24 \mu\text{m}$ " kernel to the $H\alpha$ image for NGC 3031 and the "Moffet 1.5 to $24 \mu\text{m}$ " kernel to the $H\alpha$ images for NGC 4536, NGC 5194, and NGC 7331 from the same library in the convolution process.

All the PSF-matched images have been registered on the same pixel scale ($\sim 1''.7$)¹⁰ and at the same coordinate. The image registration is conducted by using the SWarp software (Bertin et al. 2002).

3.1.4. Aperture Photometry

¹⁰ The final pixel scale of $\sim 1''.7$ is chosen for the sake of future combination with the ongoing observations by the 60/90 cm Schmidt telescope at Xing-Long station of the National Astronomical Observatories of China.

We select UV clusters representing young stellar populations inside the galaxies as our targets, which enables us to largely reduce the effects of stellar population age. The UV clusters are detected as emission peaks in the FUV images by using the SExtractor software (Bertin & Arnouts 1996). Local background subtraction is conducted to remove contamination from diffuse emission associated with evolved stellar populations. We adopt the circular median-filtering method to create local background maps for these galaxies (see Hoversten et al. 2011, for the description of this approach). Aperture photometry for the UV clusters is performed in the local-background-subtracted images. Circular apertures are adopted to extract fluxes with the radii of 8.5 arcsec for NGC 3031 and 6.8 arcsec for NGC 4536, NGC 5194, and NGC 7331, corresponding to the physical scales of 152 pc for NGC 3031, 495 pc for NGC 4536, 254 pc for NGC 5194, and 485 pc for NGC 7331, approximately. The aperture size for each galaxy is determined mainly by the spatial resolution of the images: the photometric apertures should be large enough to adequately enclose the resolved objects in each of the images and at the same time small enough to avoid as much emission from other adjacent sources as possible. The UV clusters with the measured fluxes over a 3σ level of background deviation in the FUV, NUV, $H\alpha$, $8\ \mu\text{m}$, and $24\ \mu\text{m}$ images are accepted in this work.

According to this selection, more massive clusters are supposed to be more preferentially sampled because of higher luminosities for these objects, and clusters with low mass are possibly undetected because of their luminosities below detection limits; in addition, the selected clusters in more distant galaxies ought to be systematically more massive than those in closer ones, since the photometric apertures enclose larger physical areas for more distant galaxies. As a consequence, the final sample does not contain objects with low mass in the galaxies, particularly for NGC 4536 and NGC 7331 where the mass of the selected clusters is expected to be typically more than $\sim 10^5 M_\odot$. In our work, we utilize relative quantities such as luminosity ratio and color index rather than absolute luminosity, and can thus avoid the impact of the mass of the clusters on the results.

As predicted in Section 2, heavier attenuation allows more effective discovery of the features of the attenuation curve, but the selection of UV clusters has the potential to neglect young but UV-faint regions with large amounts of dust attenuation. In case of missing this kind of sources, we additionally select IR clusters inside the galaxies as emission peaks detected in the $24\ \mu\text{m}$ images. IR clusters are also good proxies for young stellar populations as a complement of UV clusters especially for dust-obscured regions, since thermal IR radiation in galaxies, particularly with the continuum peaking at around $24\ \mu\text{m}$, is triggered by dust heating of star formation activities, and is considered to be a reliable indicator of star formation activities (Kennicutt 1998; Pérez-González et al. 2006; Calzetti et al. 2007, 2010).

Photometry is extracted for the IR clusters in the local-background-subtracted images, and the radii of photometric apertures for each galaxy are the same as in the measurements of the UV clusters. Likewise, we accept the IR clusters with the measured fluxes over a 3σ level of background deviation in each of the images. A majority of the IR clusters are the counterparts of the UV clusters with slight displacement in

the spatial position,¹¹ while there are also a few number of independent sources in the IR-selected sample.

Finally, we have 187 UV clusters and 150 IR clusters in NGC 3031, 53 UV clusters and 35 IR clusters in NGC 4536, 100 UV clusters and 117 IR clusters in NGC 5194, and 60 UV clusters and 41 IR clusters in NGC 7331 in our sample. The measured FUV and NUV fluxes for the clusters are corrected for Galactic foreground extinction through the conversion provided in Gil de Paz et al. (2007): $A_{\text{FUV}} = 7.9E(B-V)$ and $A_{\text{NUV}} = 8.0E(B-V)$, with $R_V = 3.1$. The color excess of the Galactic extinction $E(B-V)$ of each galaxy in our sample is provided by the Schlegel et al. (1998) Galactic dust map and can be directly obtained from the NASA/IPAC Extragalactic Database.¹² The measured $H\alpha$ fluxes are corrected for contamination from $[\text{NII}]\lambda\lambda 6548, 6583$ emission lines by assuming $[\text{NII}]\lambda\lambda 6548, 6583/H\alpha = 0.5$ (as suggested in Bresolin et al. 2004; Kennicutt et al. 2007, for metal-rich galaxies). All the photometric fluxes are corrected for aperture effects, following the instructions of the MIPS instrument handbook provided by the *Spitzer* Science Center.¹³ Since we have all the images identically matched with the $24\ \mu\text{m}$ PSF, the factor for the aperture correction is the same at different bands for each galaxy, depending on the aperture radius. Specifically, the aperture correction factor is 1.50 for NGC 3031, and 1.63 for NGC 4536, NGC 5194, and NGC 7331.

The broadband monochromatic luminosities are calculated according to the definition $L(\lambda) = \nu L_\nu(\lambda)$. The narrow-band $H\alpha$ luminosity is calculated by using the conversion $L(\lambda) = cL_\nu(\lambda)\Delta\lambda/\lambda^2$, where c is the speed of light and $\Delta\lambda$ is the FWHM of transmission profiles of the narrowband filters, according to the instruction in Section 7 of the SINGS user's guide.¹⁴ The total IR luminosity is derived from the $8\ \mu\text{m}$ and $24\ \mu\text{m}$ monochromatic luminosities by using Equation (1) in Calzetti et al. (2005).

Uncertainties for the photometry are estimated as a quadratic combination of the deviation of the background and the calibration uncertainties in the relevant images. The deviation of the background is introduced by the process of global and local background subtraction and derived from the global- and local-background-subtracted images. The calibration uncertainties quoted in the quadrature are 0.05 mag for FUV magnitude and 0.03 mag for NUV magnitude (Morrissey et al. 2007), 10% for $8\ \mu\text{m}$ flux (Dale et al. 2007), and 4% for $24\ \mu\text{m}$ flux (Engelbracht et al. 2007). The calibration uncertainties of the measured $H\alpha$ fluxes are 8% for NGC 3031 (Lin et al. 2003) and 10% for NGC 4536, NGC 5194, and NGC 7331 (the SINGS user's guide and Kennicutt et al. 2008).

The measured luminosities from the aperture photometry are listed in Tables 3 and 4 for the UV and IR clusters inside the galaxies respectively.

3.2. Observed IRX-UV Relation

With the measurements described above, in this subsection we present the IRX-UV diagrams for each of the galaxies and characterize the results with different signatures of the attenuation curve. Figure 4 shows the IRX-UV diagrams for the

¹¹ A similar displacement between IR and UV emission peaks inside one galaxy has been found in Calzetti et al. (2005).

¹² <http://ned.ipac.caltech.edu/>

¹³ <http://irsa.ipac.caltech.edu/data/SPITZER/docs/mips/mipsinstrumenthandbook/>

¹⁴ <http://irsa.ipac.caltech.edu/data/SPITZER/SINGS/doc/>

Table 3
Aperture Photometry of the UV Clusters

ID (Cluster Number)	R.A. ^a (J2000.0)	Dec. ^a (J2000.0)	$L(\text{FUV})^{\text{b,c,d}}$ (erg s ⁻¹)	$L(\text{NUV})^{\text{b,c,d}}$ (erg s ⁻¹)	$L(\text{H}\alpha)^{\text{b,d}}$ (erg s ⁻¹)	$L(8 \mu\text{m-dust})^{\text{b,d}}$ (erg s ⁻¹)	$L(24 \mu\text{m})^{\text{b,d}}$ (erg s ⁻¹)
NGC 3031-UV001	148.853	69.219	1.19e+40 ± 5.65e+38	9.14e+39 ± 2.91e+38	4.29e+37 ± 8.08e+36	5.71e+38 ± 9.51e+37	1.61e+38 ± 2.68e+37
NGC 3031-UV002	148.755	69.216	6.61e+39 ± 3.18e+38	4.88e+39 ± 1.95e+38	2.48e+38 ± 1.81e+37	5.27e+39 ± 5.32e+38	2.96e+39 ± 1.21e+38
NGC 3031-UV003	148.770	69.214	1.89e+39 ± 1.11e+38	1.27e+39 ± 1.43e+38	3.88e+37 ± 7.98e+36	1.70e+39 ± 1.86e+38	6.07e+38 ± 3.56e+37
...							
NGC 4536-UV001	188.586	2.220	2.98e+40 ± 1.54e+39	2.43e+40 ± 9.39e+38	3.79e+37 ± 7.86e+36	1.37e+40 ± 2.12e+39	2.69e+39 ± 6.73e+38
NGC 4536-UV002	188.576	2.223	4.46e+40 ± 2.20e+39	3.72e+40 ± 1.23e+39	7.07e+37 ± 9.72e+36	1.75e+40 ± 2.39e+39	4.88e+39 ± 6.92e+38
NGC 4536-UV003	188.579	2.221	1.05e+41 ± 4.98e+39	8.37e+40 ± 2.43e+39	2.43e+38 ± 2.43e+37	3.54e+40 ± 3.89e+39	1.31e+40 ± 8.47e+38
...							
NGC 5194-UV001	202.481	47.111	6.45e+39 ± 1.08e+39	4.97e+39 ± 1.17e+39	2.13e+38 ± 3.02e+37	1.60e+40 ± 2.93e+39	3.89e+39 ± 9.24e+38
NGC 5194-UV002	202.516	47.265	2.33e+40 ± 1.51e+39	2.19e+40 ± 1.31e+39	2.24e+38 ± 3.08e+37	1.71e+40 ± 3.00e+39	6.43e+39 ± 9.47e+38
NGC 5194-UV003	202.515	47.263	3.14e+40 ± 1.80e+39	2.68e+40 ± 1.38e+39	6.60e+38 ± 6.50e+37	4.52e+40 ± 5.14e+39	2.39e+40 ± 1.32e+39
...							
NGC 7331-UV001	339.257	34.481	4.08e+40 ± 2.02e+39	3.42e+40 ± 1.32e+39	8.21e+38 ± 7.14e+37	3.26e+40 ± 5.26e+39	1.10e+40 ± 1.40e+39
NGC 7331-UV002	339.271	34.472	9.14e+39 ± 7.68e+38	8.19e+39 ± 9.36e+38	1.66e+38 ± 2.93e+37	1.73e+40 ± 4.47e+39	4.64e+39 ± 1.34e+39
NGC 7331-UV003	339.246	34.462	1.81e+40 ± 1.07e+39	1.38e+40 ± 9.86e+38	2.88e+38 ± 3.50e+37	3.81e+40 ± 5.62e+39	5.07e+39 ± 1.34e+39
...							

Note. — The aperture radius is 8".5 for NGC 3031, and 6".8 for NGC 4536, NGC 5194, and NGC 7331. This table is available in its entirety in the online journal. A portion is shown here for guidance regarding its form and content.

^a Position of the apertures on the sky.

^b Luminosities measured after local background subtraction.

^c Luminosities corrected for Galactic foreground extinction.

^d Luminosities corrected for aperture effects.

Table 4
Aperture Photometry of the IR Clusters

ID (Cluster Number)	R.A. ^a (J2000.0)	Dec. ^a (J2000.0)	$L(\text{FUV})^{\text{b,c,d}}$ (erg s ⁻¹)	$L(\text{NUV})^{\text{b,c,d}}$ (erg s ⁻¹)	$L(\text{H}\alpha)^{\text{b,d}}$ (erg s ⁻¹)	$L(8 \mu\text{m-dust})^{\text{b,d}}$ (erg s ⁻¹)	$L(24 \mu\text{m})^{\text{b,d}}$ (erg s ⁻¹)
NGC 3031-IR001	148.749	69.237	4.31e+39 ± 2.14e+38	3.36e+39 ± 1.68e+38	4.72e+37 ± 8.18e+36	1.31e+39 ± 1.51e+38	8.42e+38 ± 4.25e+37
NGC 3031-IR002	148.756	69.216	6.32e+39 ± 3.05e+38	4.63e+39 ± 1.90e+38	2.39e+38 ± 1.76e+37	5.23e+39 ± 5.28e+38	2.97e+39 ± 1.21e+38
NGC 3031-IR003	148.769	69.214	1.99e+39 ± 1.15e+38	1.33e+39 ± 1.44e+38	4.22e+37 ± 8.06e+36	1.83e+39 ± 1.98e+38	6.62e+38 ± 3.71e+37
...							
NGC 4536-IR001	188.580	2.221	9.91e+40 ± 4.71e+39	8.09e+40 ± 2.36e+39	2.38e+38 ± 2.39e+37	3.27e+40 ± 3.65e+39	1.26e+40 ± 8.34e+38
NGC 4536-IR002	188.576	2.215	4.80e+40 ± 2.35e+39	4.35e+40 ± 1.38e+39	1.14e+38 ± 1.30e+37	5.68e+40 ± 5.91e+39	2.42e+40 ± 1.17e+39
NGC 4536-IR003	188.581	2.207	3.19e+40 ± 1.63e+39	3.38e+40 ± 1.15e+39	1.36e+38 ± 1.48e+37	6.95e+40 ± 7.13e+39	2.14e+40 ± 1.08e+39
...							
NGC 5194-IR001	202.482	47.112	6.24e+39 ± 1.07e+39	4.88e+39 ± 1.17e+39	2.09e+38 ± 2.99e+37	1.67e+40 ± 2.97e+39	4.05e+39 ± 9.25e+38
NGC 5194-IR002	202.509	47.269	5.56e+39 ± 1.06e+39	3.88e+39 ± 1.16e+39	1.18e+38 ± 2.53e+37	2.42e+40 ± 3.45e+39	7.83e+39 ± 9.63e+38
NGC 5194-IR003	202.515	47.263	3.14e+40 ± 1.80e+39	2.72e+40 ± 1.38e+39	6.23e+38 ± 6.18e+37	4.20e+40 ± 4.87e+39	2.18e+40 ± 1.26e+39
...							
NGC 7331-IR001	339.287	34.342	2.90e+40 ± 1.51e+39	2.85e+40 ± 1.21e+39	2.04e+38 ± 3.09e+37	3.37e+40 ± 5.33e+39	7.97e+39 ± 1.37e+39
NGC 7331-IR002	339.257	34.482	3.65e+40 ± 1.83e+39	3.05e+40 ± 1.25e+39	7.67e+38 ± 6.74e+37	4.08e+40 ± 5.80e+39	1.30e+40 ± 1.43e+39
NGC 7331-IR003	339.271	34.472	8.38e+39 ± 7.49e+38	7.66e+39 ± 9.33e+38	1.62e+38 ± 2.92e+37	1.69e+40 ± 4.46e+39	4.64e+39 ± 1.34e+39
...							

Note. — The aperture radius is 8".5 for NGC 3031, and 6".8 for NGC 4536, NGC 5194, and NGC 7331. This table is available in its entirety in the online journal. A portion is shown here for guidance regarding its form and content.

^a Position of the apertures on the sky.

^b Luminosities measured after local background subtraction.

^c Luminosities corrected for Galactic foreground extinction.

^d Luminosities corrected for aperture effects.

measured clusters inside NGC 3031, NGC 4536, NGC 5194, and NGC 7331, where we adopt the MW, M-S, and SMC curves to offer model comparisons. Two stellar population ages, 2 Myr and 100 Myr, are employed to frame a potential range of age scatter in this relation and describe the envelope of the distribution for objects with the maximal age of 100 Myr in the IRX-UV plane. As shown in this figure, aging from 2 to 100 Myr of simple stellar populations introduces a

redward shift by ~ 0.5 mag in FUV – NUV at fixed IRX.¹⁵

In the top left panel of Figure 4, the clusters inside NGC 3031 lie in a range from -0.2 to 0.5 mag in FUV – NUV and from -1.0 to 1.0 in IRX, possessing nearly constant FUV – NUV space albeit with different IRX. The weak reddening of FUV – NUV with increasing IRX coincides with the impact of the 2175 Angstrom bump. The presence of a

¹⁵ In this work, we employ simple stellar populations born with an instantaneous burst in spectral synthesis modeling, in order to illuminate the maximal impact of stellar population age. More complex SFHs are supposed to disperse the age effects, as presented in Paper I.

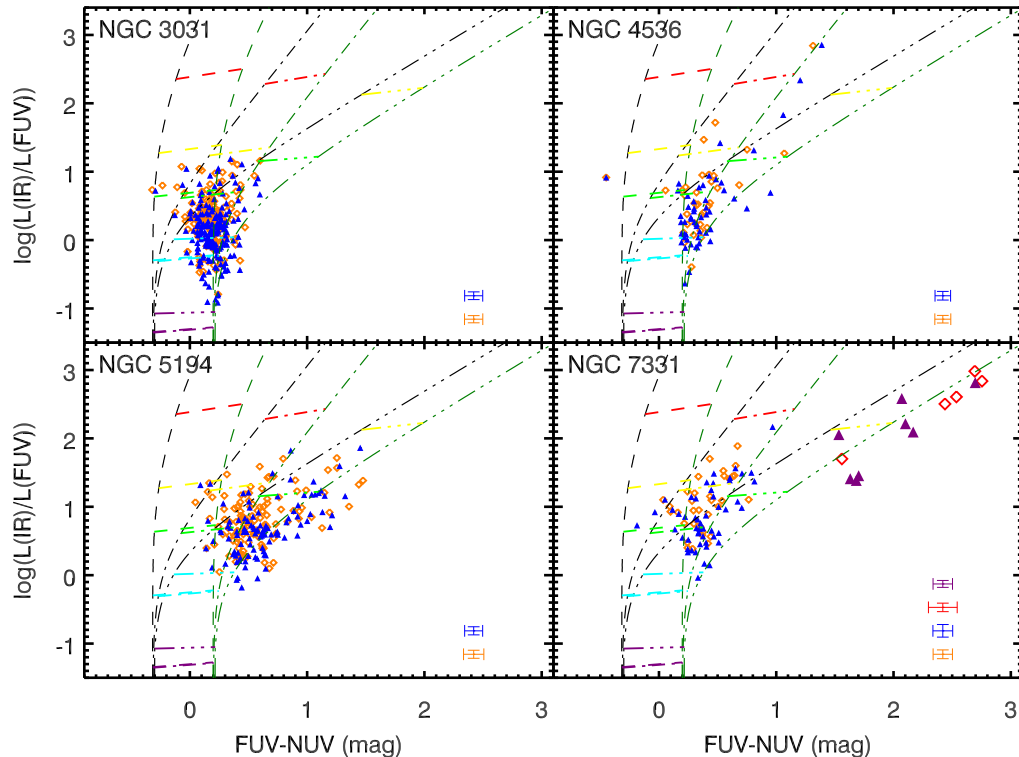


Figure 4. IRX vs. FUV–NUV for the UV clusters (blue filled triangles) and the IR clusters (orange open diamonds) inside NGC 3031 (top left panel), NGC 4536 (top right panel), NGC 5194 (bottom left panel), and NGC 7331 (bottom right panel). For NGC 7331, the UV and the IR clusters in the central ring are further marked in purple and red, respectively, with larger symbols. The lines superimposed on each panel are obtained by spectral synthesis modeling with different attenuation curves: the MW curve (dashed line), the M-S curve (dot-dashed line), and the SMC curve (triple-dot-dashed line), and they are color-coded by stellar population age: 2 Myr (black) and 100 Myr (dark green). The points of five constant amounts of dust attenuation on the IRX-UV tracks modeled with the same attenuation curve but different stellar population ages are connected by lines with different colors: $A(V) = 0.01$ (purple), 0.1 (cyan), 0.5 (green), 1.0 (yellow), and 2.0 (red) mag. The median errors for the UV clusters (blue) and the IR clusters (orange) are plotted at the bottom right corner of each panel, and for NGC 7331 the error bars are plotted for the disk UV clusters (blue), the disk IR clusters (orange), the ring UV clusters (purple), and the ring IR cluster (red).

prominent 2175 Angstrom bump in the attenuation curve provides an interpretation better than the scenarios designed with the bumpless C00 curve in Paper I. However, a majority of the clusters in NGC 3031 are located below $IRX = 0.5$, and the distinction between different attenuation curves is nearly invisible in this range where the deviation in the IRX-UV relation is more likely ascribed to other effects such as the aging of stellar populations.

Contrary to the narrow IRX and color ranges for NGC 3031, the IRX-UV relation for NGC 4536 presents obvious reddening in FUV–NUV with increasing IRX, as shown in the top right panel of Figure 4. The clusters span a wide range from 0.0 to 1.4 mag in FUV–NUV and from -0.7 to 2.9 in IRX. In this diagram, the M-S curve depicts a similar trend to the data distribution. From the right panel of Figure 3, we can see that the M-S curve and the C00 curve reproduce the comparable IRX-UV tracks, and this consistency hints at the reason why the scenarios designed with the C00 curve were applicable to NGC 4536 in Paper I. Furthermore, the tentative analysis based on the three template attenuation curves in this paper implies a bumpless attenuation curve with the MW-type slope for this galaxy.

The reddening inclination of the IRX-UV relation with increasing IRX can also be seen from the bottom left panel of Figure 4 for NGC 5194, but the trend appears to be more intensive, i.e., redder FUV–NUV at constant IRX than the re-

sult from NGC 4536. The data points from NGC 5194 cover the space between the M-S curve and the SMC curve in this diagram. In Paper I, the scenarios with the C00 curve overestimated the stellar population ages for about half of the UV clusters inside NGC 5194, while in this paper, an interpretation with steeper attenuation curves helps to avoid the problem.

The bottom right panel of Figure 4 shows the IRX-UV diagram for NGC 7331. For this galaxy, because of the presence of the IR-prominent ring residing in its central area (Regan et al. 2004; Thilker et al. 2007, and Paper I), we further divide the measured clusters into disk clusters and ring clusters in order to distinguish their respective features. In this diagram, the disk clusters lie in the range of about 0.0–1.0 mag in FUV–NUV and 0.0–2.0 in IRX, and the ring clusters are located in the range of 1.5–2.8 mag in FUV–NUV and 1.3–3.0 in IRX. The high levels of IRX and the serious reddening of FUV–NUV for the ring clusters are assumed to be an aftermath of dust-rich properties in the ring area. It is obvious to see that the disk clusters and the ring clusters possess separate regimes in the IRX-UV plane: the disk clusters appear to follow the relation reproduced by the M-S curve, whereas the ring clusters distribute along the tracks built by the SMC curve. In Paper I, the scenarios modeled with the C00 curve also overestimates stellar population age for the subregions in the ring area of NGC 7331, while in this paper,

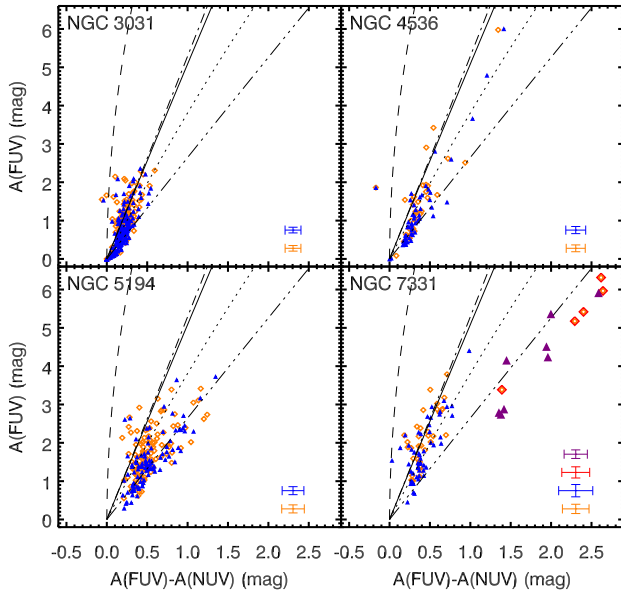


Figure 5. FUV attenuation as a function of UV color excess for the individual galaxies in our sample. The symbols are the same as those assigned in Figure 4. The FUV and NUV attenuations are estimated on the basis of the B05 calibration. The lines superimposed on each diagram describe the relations modeled with the MW curve (dashed line), the M-S curve (dot-dashed line), the SMC curve (triple-dot-dashed line), the S-M curve (dotted line), and the C00 curve (solid line). The median errors for the UV clusters (blue) and the IR clusters (orange) are plotted at the bottom right corner of each panel, and for NGC 7331 the error bars are plotted for the disk UV clusters (blue), the disk IR clusters (orange), the ring UV clusters (purple), and the ring IR cluster (red).

a steeper attenuation curve such as the SMC curve offers a more suitable interpretation of the data locus.

3.3. Diagnosis of the Attenuation Curve

We have studied the IRX-UV distributions coincident with the features of the typical attenuation curves by taking each galaxy as a unit in the above section. However, this investigation does not mean that we intentionally presume one constant attenuation curve for a given galaxy. As a matter of fact, the attenuation curve is indeed likely to vary between subregions within one galaxy. In this subsection, we attempt to diagnose the signatures of attenuation curve for each of the galaxies independently of any presumption. A comparison between attenuations at different wavelength bands is the most feasible approach to probing attenuation curve if spectral observations are not available. As the first step, we compare FUV and NUV attenuations ($A(\text{FUV})$ and $A(\text{NUV})$) for the measured clusters inside the galaxies.

The observed $A(\text{FUV})$ and $A(\text{NUV})$ for the clusters are derived from $\log(L(\text{IR})/L(\text{FUV}))$ and $\log(L(\text{IR})/L(\text{NUV}))$, respectively, on the basis of the energy balance principle (Xu & Buat 1995; Buat & Xu 1996) and the calibration addressed in Buat et al. (2005, hereafter denoted as B05):

$$A(\text{FUV}) = -0.0333x_1^3 + 0.3522x_1^2 + 1.1960x_1 + 0.4967, \quad (4)$$

and

$$A(\text{NUV}) = -0.0495x_2^3 + 0.4718x_2^2 + 0.8998x_2 + 0.2269, \quad (5)$$

where $x_1 \equiv \log(L(\text{IR})/L(\text{FUV}))$ and $x_2 \equiv \log(L(\text{IR})/L(\text{NUV}))$. Equations (4) and (5) offer a for-

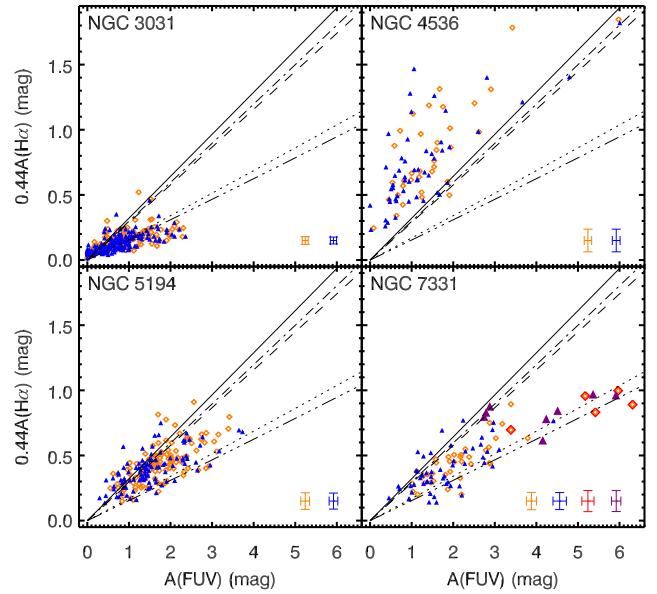


Figure 6. $H\alpha$ continuum attenuation as a function of FUV attenuation for the individual galaxies in our sample. The symbols are the same as those assigned in Figure 4. The FUV attenuation is estimated on the basis of the B05 calibration, and the $H\alpha$ attenuation is obtained by using the calibration in Calzetti et al. (2007). The lines superimposed on each diagram describe the relations modeled with the MW curve (dashed line), the M-S curve (dot-dashed line), the SMC curve (triple-dot-dashed line), the S-M curve (dotted line), and the C00 curve (solid line). The median errors for the UV clusters (blue) and the IR clusters (orange) are plotted at the bottom right corner of each panel, and for NGC 7331 the error bars are plotted for the disk UV clusters (blue), the disk IR clusters (orange), the ring UV clusters (purple), and the ring IR cluster (red).

mula for estimating FUV and NUV attenuations that is not biased by any specific attenuation curve and consequently suitable for the diagnosis of the attenuation curve in our work. The reliability of the B05 formula will be examined in detail in Section 4.

Although there should be no theoretical effect of stellar population age on the relationship between $A(\text{FUV})$ and $A(\text{NUV})$, the estimators $\log(L(\text{IR})/L(\text{FUV}))$ and $\log(L(\text{IR})/L(\text{NUV}))$ are not definitely independent of stellar population age (Cortese et al. 2008). In Figure 4, the lines connecting constant attenuation points on the IRX-UV tracks for different ages indicate a very slight difference in IRX between 2 and 100 Myr for the same attenuation; however, the diagnosis based on the comparison between $A(\text{FUV})$ and $A(\text{NUV})$ can still be possibly affected by this age effect. Via an examination with stellar population synthesis modeling, we find that the application of Equations (4) and (5) to stellar populations within an age interval of 2–100 Myr would introduce a certain degree of scatter less than ~ 0.4 mag in $A(\text{FUV}) - A(\text{NUV})$ at fixed $A(\text{FUV})$. The influence of this scatter on the diagnosis of the attenuation curve is trivial at a large amount of attenuation but is considerable for objects with low dust content. A more detailed discussion about this effect will be addressed in Section 5.2.

The comparison between $A(\text{FUV})$ and $A(\text{NUV})$ is shown in Figure 5 for the clusters inside NGC 3031, NGC 4536, NGC 5194, and NGC 7331, and the tracks reproduced by the MW curve, the M-S curve, the SMC curve, the S-M curve, and the C00 curve are superimposed on each panel

of this figure as well. The modeled lines indicate a trend of decreasing $A(\text{NUV})$ at constant $A(\text{FUV})$ with weaker bump strength or steeper linear background. A majority of the clusters inside NGC 3031 populate in the range of 0.0–2.5 mag in $A(\text{FUV})$ and 0.0–0.5 mag in $A(\text{FUV}) - A(\text{NUV})$, and they appear with quite a small change in $A(\text{FUV})$ and $A(\text{NUV})$ at the low attenuation level. The clusters inside NGC 4536 present a tight correlation extending to $A(\text{FUV}) \sim 6.0$ mag and $A(\text{FUV}) - A(\text{NUV}) \sim 1.5$ mag, and they require a bumpless feature or/and a steeper linear background in the attenuation curve that is different from the MW-type feature to characterize the distribution. Most of the data points from NGC 5194 span about 1.5 mag in $A(\text{FUV}) - A(\text{NUV})$ within $A(\text{FUV}) < 4.0$ mag and fall into the transitional space between the M-S curve and the SMC curve, suggesting a bumpless attenuation curve with the slope valuated between the MW and SMC types. For NGC 7331, we can clearly see the different behaviors between the disk and the ring clusters in the diagram: the disk clusters follow the M-S curve in the range of 0.5–4.0 mag in $A(\text{FUV})$ and 0.0–1.0 mag in $A(\text{FUV}) - A(\text{NUV})$ approximately, whereas the ring clusters follow the SMC curve at higher levels of both attenuation and reddening, $2.5 < A(\text{FUV}) < 6.3$ mag and $1.2 < A(\text{FUV}) - A(\text{NUV}) < 2.7$ mag.

As we have implied at the end of Section 2, there is a degeneracy of the linear background and the 2175 Angstrom bump in NUV attenuation, which makes it impossible to estimate the attenuation curve by adopting only UV wavelength bands. The track reproduced by the S-M curve is displayed in Figure 5 as an example of this degeneracy to illustrate the same appearance produced by different combinations of the linear background slope and the bump strength in the $A(\text{FUV})$ versus $A(\text{NUV})$ diagnostics. In this situation, it is necessary to have more observational tracers of the parameters in the attenuation curve.

The $\text{H}\alpha$ emission line resides at the wavelength of $\lambda \sim 6563$ Angstrom beyond the coverage of the 2175 Angstrom bump; therefore, it is in a good position to offer a complementary diagnosis, especially for the linear background slope.

$\text{H}\alpha$ emission lines are ionized from gaseous nebulae by young and massive stars in star-forming regions. The same star formation activities also heat interstellar dust grains to high temperatures (> 100 K) and excite IR continua peaking at around $24 \mu\text{m}$ from the dust. The common association of $\text{H}\alpha$ and $24 \mu\text{m}$ emission with star formation leads to a correlation between intrinsic (unattenuated) $\text{H}\alpha$ and $24 \mu\text{m}$ luminosities, i.e., if there is no attenuation, the ratio of $24 \mu\text{m}$ to $\text{H}\alpha$ luminosities is supposed to be constant. As a result, the combination of observed (attenuated) $\text{H}\alpha$ with $24 \mu\text{m}$ luminosities is proposed as a robust estimator of $\text{H}\alpha$ attenuation, i.e., theoretically, the difference of the observed $24 \mu\text{m}$ -to- $\text{H}\alpha$ ratio from its intrinsic value is ascribed to $\text{H}\alpha$ attenuation (Pérez-González et al. 2006; Calzetti et al. 2007; Relaño et al. 2007; Kennicutt et al. 2007, 2009). Compared with UV or optical blue-band attenuation, $\text{H}\alpha$ attenuation is insensitive to variations in the attenuation curve since the differences between various attenuation curves are quite slight in long wavelength bands. This property implies that the calibration of the $24 \mu\text{m}$ -to- $\text{H}\alpha$ ratio to $\text{H}\alpha$ attenuation is not biased by any certain form of the attenuation curve.

In terms of the $24 \mu\text{m}$ -to- $\text{H}\alpha$ ratio, $\text{H}\alpha$ attenuation is ex-

pressed as follows:

$$A(\text{H}\alpha) = 2.5 \log\left(1 + \frac{aL(24 \mu\text{m})}{L(\text{H}\alpha)_{\text{obs}}}\right). \quad (6)$$

We adopt this formula to estimate $\text{H}\alpha$ attenuation for the clusters inside the galaxies in our work, with the scaling factor of $a = 0.031 \pm 0.006$ according to the calibration for HII regions inside nearby galaxies addressed in Calzetti et al. (2007).¹⁶

With $\text{H}\alpha$ attenuation derived as described above, we employ the combination of FUV and $\text{H}\alpha$ attenuations to probe the linear background slope. Figure 6 shows $0.44A(\text{H}\alpha)$ as a function of $A(\text{FUV})$ for the galaxies in our sample, where $0.44A(\text{H}\alpha)$ is defined to convert the attenuation of the $\text{H}\alpha$ emission line to the attenuation of the stellar continuum at the $\text{H}\alpha$ band (~ 6563 Angstrom), and stellar continuum attenuation at $\text{H}\alpha$ band is defined as $A(6563)$. The conversion $A(6563) = 0.44A(\text{H}\alpha)$ is applied to our work on the basis of the definition $E(B - V)_{\text{star}} = 0.44E(B - V)_{\text{gas}}$ in Calzetti (1997) together with the assumption of a common attenuation law for stars and gas populating the same subregion inside one galaxy. The lines superimposed on each panel of this figure are reproduced by the MW curve (with the MW-type slope), the M-S curve (with the MW-type slope), the SMC curve (with the SMC-type slope), the S-M curve (with the SMC-type slope), and the C00 curve. These modeled lines indicate a clear separation between different slopes in the attenuation curve, and at the same time they present tight overlaps between the attenuation curves with the same slope albeit different bump strengths, e.g., the MW curve overlaps with the M-S curve, and the SMC curve overlaps with the S-M curve.¹⁷ As illustrated in this figure, the steeper slope leads to higher $A(\text{FUV})$ at constant $A(\text{H}\alpha)$ compared with the shallower slope. This disparity between different slopes becomes more extensive as attenuation increases, and when $0.44A(\text{H}\alpha) > 0.44$ mag (i.e., $A(\text{H}\alpha) > 1.0$ mag), the difference between $A(\text{FUV})$ reproduced by the MW- and the SMC-type slopes extends to over 1.0 mag.

In the top left panel of Figure 6, most of the data points from NGC 3031 lie in $A(\text{FUV}) < 2.0$ mag and $0.44A(\text{H}\alpha) < 0.3$ mag. The low level of attenuation hampers strict constraints on the form of the attenuation curve for this galaxy. Nevertheless, the $A(\text{H}\alpha)$ versus $A(\text{FUV})$ relation does not show an evident trend of the linear background being shallower than the MW-type slope, and in order to fulfill the $A(\text{FUV})$ versus $A(\text{FUV}) - A(\text{NUV})$ distribution in Figure 5, the presence of a prominent 2175 Angstrom bump is assumed in the attenuation curve for NGC 3031.

For NGC 4536, in the top right panel of Figure 6, the galactic core is located at $A(\text{FUV}) \sim 6.0$ mag and $0.44A(\text{H}\alpha) \sim 1.8$ mag. Other data points from this galaxy span about 1.5 mag in $0.44A(\text{H}\alpha)$ within the range of ~ 4.0 mag in $A(\text{FUV})$, and they present a larger amount of $\text{H}\alpha$ -band continuum at-

¹⁶ Alternatively, Kennicutt et al. (2007) have found a best-fitting value of $a = 0.038 \pm 0.005$ for HII regions inside a specific galaxy NGC 5194, which is comparable to the Calzetti et al. (2007) calibration, and adopting this value does not impose any effective bias on the results in this paper. Kennicutt et al. (2009) have derived $a = 0.020 \pm 0.005$ from integrated measurements of nearby galaxies, and this value is inappropriate for our work, because of the different stellar populations contained in the young clusters studied in this paper and the galaxies as a whole sampled in Kennicutt et al. (2009).

¹⁷ In Figure 6, we can see slight displacement in each overlap, which is due to the blueward tail of the 2175 Angstrom bump extending to the FUV band-pass. But compared with the separation, the displacements are very trivial and negligible.

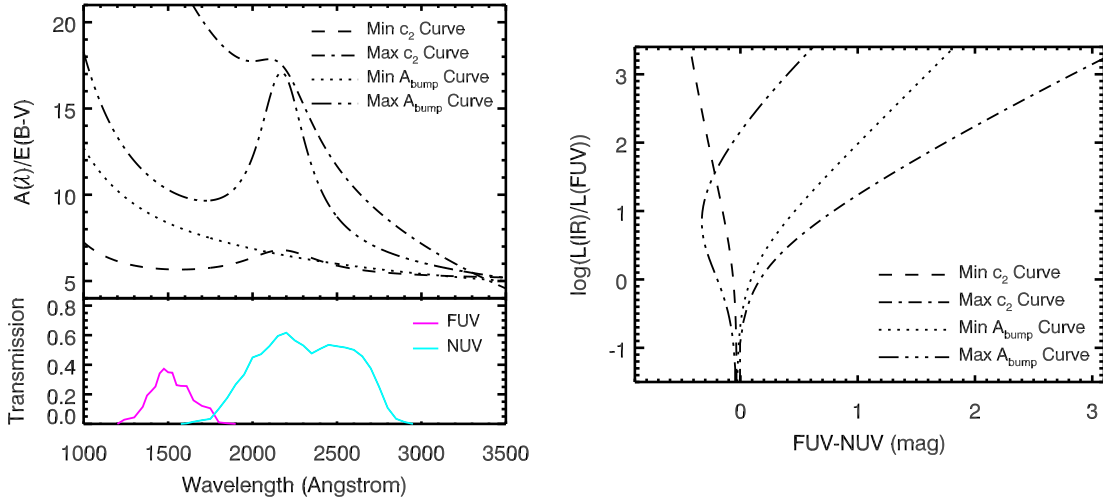


Figure 7. Left: four extreme attenuation curves in the artificial sample with the minimal c_2 (dashed line; $c_2 = 0.100$, $c_3 = 1.949$, $c_4 = 0.107$, $\gamma = 1.301$), the maximal c_2 (dot-dashed line; $c_2 = 5.000$, $c_3 = 3.971$, 0.349 , $\gamma = 0.898$), the minimal A_{bump} (dotted line; $c_2 = 0.872$, $c_3 = 0.0$, $c_4 = 0.115$, $\gamma = 0.830$), and the maximal A_{bump} (triple-dot-dashed line; $c_2 = 1.273$, $c_3 = 4.996$, $c_4 = 0.321$, $\gamma = 0.503$). Filter transmission curves of the GALEX FUV (magenta) and NUV (cyan) bands are also shown. Right: IRX-UV tracks reproduced with the attenuation curves shown in the left panel.

tenuation at constant $A(\text{FUV})$ than the expectation from the MW-type slope (or the C00 curve). In this case, the locus appears to reflect the linear background shallower than the MW-type slope. However, the relation between $A(\text{FUV})$ and $A(\text{FUV}) - A(\text{NUV})$ for NGC 4536 in Figure 5 requires the MW-type slope with no bump, or steeper slope with a certain degree of bumps in the attenuation curve. Otherwise, the linear background shallower than the MW-type slope has to result in a bump with negative strength, as can be deduced from the combination of Figures 5 and 6. This discrepancy possibly comes from the estimates of $H\alpha$ attenuation, ascribed to differences in the conversion factor from 0.44 (which will be discussed in Section 5.3), or/and different intrinsic values of $24 \mu\text{m}$ -to- $H\alpha$ ratio (which will be discussed in Section 5.4), where the former potentially affects the results for all the galaxies in our work, and the latter is suspected to take place in NGC 4536. Despite the problem in the diagnosis of the linear background for NGC 4536, we do not find any evidence of the linear background in the attenuation curve steeper than the MW type, and also the suggestion of a bumpless feature in the attenuation curve is more apt for this galaxy.

The distribution of the clusters inside NGC 5194 approximates in the range of 0.0–4.0 mag in $A(\text{FUV})$ and 0.0–1.0 mag in $0.44A(H\alpha)$, which is well interpreted with the linear background slope between the MW and SMC types, as shown in the bottom left panel of Figure 6. This diagnosis in combination with the result from Figure 5 strengthens the suggestion of the bumpless feature in the attenuation curve for this galaxy.

The correlation between $A(H\alpha)$ and $A(\text{FUV})$ for NGC 7331 is shown in the bottom right panel of Figure 6. The disk clusters populate in $A(\text{FUV}) < 4.0$ mag and $0.44A(H\alpha) < 0.9$ mag space, while the ring clusters are located at higher attenuation levels of about 3.0–6.3 mag in $A(\text{FUV})$ and 0.5–1.0 mag in $0.44A(H\alpha)$. A number of data points from the disk and the ring appear to possess a common regime between the MW- and SMC-type slopes. By taking the separate distributions between the disk and ring points in Figure 5 into consideration, the ring clusters can be confirmed to have a bumpless feature (or a very trivial bump if any) in the attenuation curve,

whereas the disk clusters are suggested as having a similar slope but a prominent bump in order to better fit the relatively smaller differences between $A(\text{FUV})$ and $A(\text{NUV})$ than the ring clusters shown in Figure 5.

4. INVESTIGATION WITH AN ARTIFICIAL SAMPLE

In the above sections, the linear background and the 2175 Angstrom bump are expected to have significant impacts on the IRX-UV relation, and the observational features of the two parameters are diagnosed for the galaxies studied in this paper. In this section, by constructing an artificial sample to simulate observational data, we will investigate the observability of the presented features, assess the reliability of the applied diagnostics, and propose a prescription for quantitative constraints on the parameters in the attenuation curve.

4.1. Artificial Sample

We employ the models of the stellar population synthesis described in Section 2 with a variety of attenuation curves to produce 20000 mock objects that compose a mock catalog. In this catalog, values for each physical parameter are randomly generated and uniformly distributed in a certain range, including stellar population age from 2 to 100 Myr, $0.0 < A(V) \leq 3.0$ mag, $0.1 \leq c_2 \leq 5.0$, $0.0 \leq c_3 \leq 5.0$, $0.0 \leq c_4 \leq 0.5$, and $0.5 \leq \gamma \leq 1.5 \mu\text{m}^{-1}$ (see similar methods introduced in Kauffmann et al. 2003; Kong et al. 2004; Lin et al. 2013).

This artificial sample, for the purpose of reproducing attenuation features that potentially exist in young clusters inside galaxies, only contains young and simple stellar populations (≤ 100 Myr); older or more composite stellar populations are not adopted. The $A(V)$ up to 3.0 mag suffices to fit most observations. The ranges for the coefficients in the FM parameterization of the attenuation curve, i.e., c_2 , c_3 , c_4 , and γ , are determined in consideration of the realistic observations (Fitzpatrick & Massa 1988, 1990; Gordon et al. 2003). The stellar populations in this catalog are assumed to be born from an instantaneous burst with the Kroupa (2002) initial mass function (with exponents of 1.3 over 0.1 – $0.5 M_{\odot}$ and 2.3 over 0.5 – $100 M_{\odot}$) and solar metallicity.

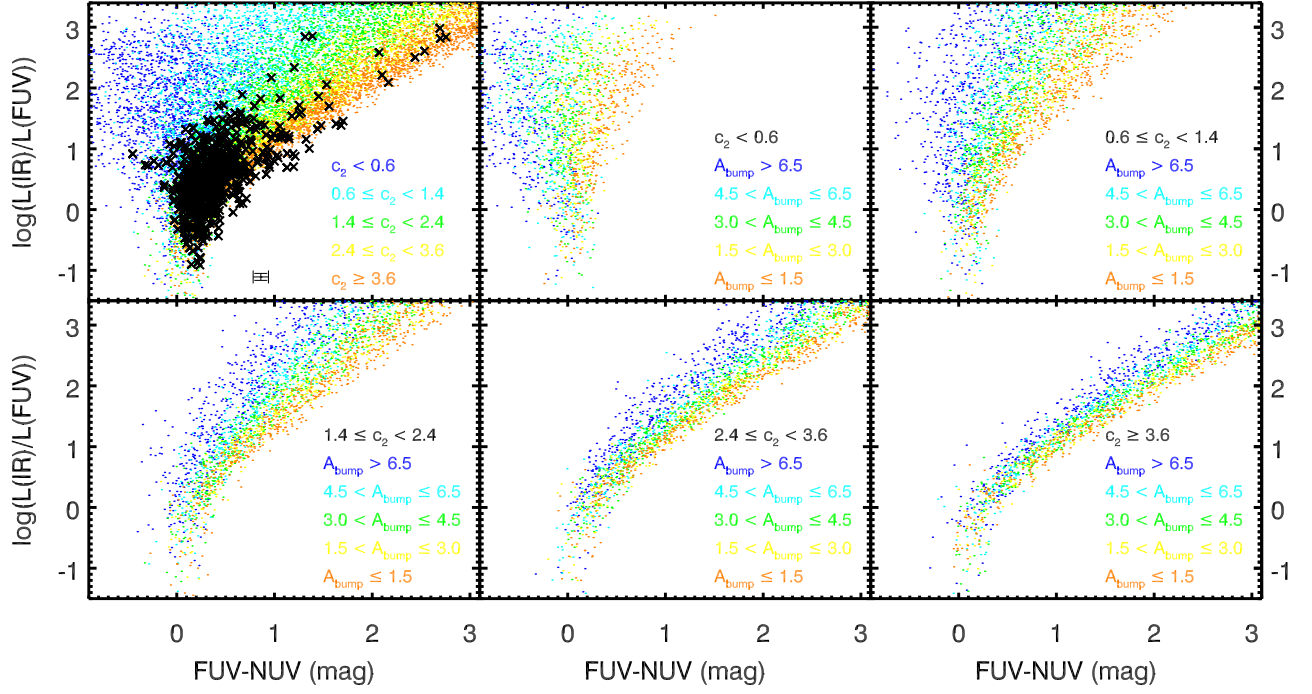


Figure 8. IRX vs. FUV–NUV for the artificial sample described in Section 4. In the top left panel, the points in the entire sample are color-coded by c_2 : $c_2 < 0.6$ (blue), $0.6 \leq c_2 < 1.4$ (cyan), $1.4 \leq c_2 < 2.4$ (green), $2.4 \leq c_2 < 3.6$ (yellow), and $c_2 \geq 3.6$ (orange); black crosses superimposed on this panel represent all the clusters inside the four galaxies described in Section 3; and the error bar plotted at the bottom of this panel shows the median uncertainties for the clusters. The other five panels show IRX as a function of FUV–NUV for the subsample with $c_2 < 0.6$ (top middle panel, corresponding to the blue points in the top left panel), $0.6 \leq c_2 < 1.4$ (top right panel, corresponding to the cyan points in the top left panel), $1.4 \leq c_2 < 2.4$ (bottom left panel, corresponding to the green points in the top left panel), $2.4 \leq c_2 < 3.6$ (bottom middle panel, corresponding to the yellow points in the top left panel), and $c_2 \geq 3.6$ (bottom right panel, corresponding to the orange points in the top left panel). The points in each subsample are color-coded by A_{bump} : $A_{\text{bump}} > 6.5$ (blue), $4.5 < A_{\text{bump}} \leq 6.5$ (cyan), $3.0 < A_{\text{bump}} \leq 4.5$ (green), $1.5 < A_{\text{bump}} \leq 3.0$ (yellow), and $A_{\text{bump}} \leq 1.5$ (orange).

UV and IR luminosities for the mock objects are obtained, respectively, through the convolution of the modeled spectra with filter transmission curves and the sum of attenuated stellar emission, which is the same as described in Section 2. Uncertainties are also simulated and assigned to the quantities in the artificial sample, and at this step, we assume a normal distribution with the standard deviation defined as the median values of the photometric uncertainties in the observational data described in Section 3.1.

The investigation with the mock catalog will focus on c_2 and A_{bump} ($\equiv \pi c_3 / (2\gamma)$, the area enclosed by the 2175 Angstrom bump in the attenuation curve) and involve an elaborate analysis of the roles played by both parameters in the IRX–UV relation. Figure 7 is displayed as a preview to show the extreme attenuation curves with minimal and maximal c_2 and A_{bump} in the artificial sample respectively, and the IRX–UV tracks reproduced with these attenuation curves. The following subsections will present the investigation with all the attenuation curves of high diversity in the artificial sample.

4.2. Simulated IRX–UV Relation

Figure 8 shows the IRX–UV diagrams for the artificial sample and its different ingredients. The top left panel of this figure presents the result for the entire sample, where the mock objects are color-coded by different c_2 ranges, and the observational data (the clusters inside the galaxies) are superimposed on the diagram in order to show the artificial sample covering the observations in the IRX–UV plane; the other five panels exhibit the results for the five subsamples of the mock

objects that correspond, respectively, to the five c_2 bins defined in the top left panel, where the data points are color-coded by different A_{bump} ranges.

In the top left panel of Figure 8, the entire sample spreads in a broad range in the IRX–UV diagram and possesses more extended FUV–NUV space with increasing IRX. By means of the color-coding, we can see a clear trend of the overall data distribution with c_2 : the objects with larger c_2 tend to incline toward redder FUV–NUV at fixed IRX. However, this trend presents considerable dispersion on local scales, where the loci for different c_2 bins overlap seriously with each other. This dispersion is interpreted in the other panels of Figure 8 by further categorizing each of the subsamples into different A_{bump} bins: in addition to c_2 , A_{bump} affects the IRX–UV relation at the same time but in an opposite direction, displayed as a blueing of the UV color at constant IRX. These results clearly illustrate that both of c_2 and A_{bump} are able to have significant impacts on the locations of data points in the IRX–UV planes, whereas the degeneracy of the two parameters, in turn, is likely to disperse the visible signatures of any single parameter.

4.3. Constraints on the Attenuation Curve

The combination of FUV, NUV, and $H\alpha$ -band continuum attenuations is a feasible way to estimate the linear background slope and the 2175 Angstrom bump strength, as suggested in Section 3.3. In this subsection, we make use of the artificial sample to thoroughly investigate the correlations of c_2 and A_{bump} with $A(\text{FUV})$, $A(\text{NUV})$, and $H\alpha$ -band contin-

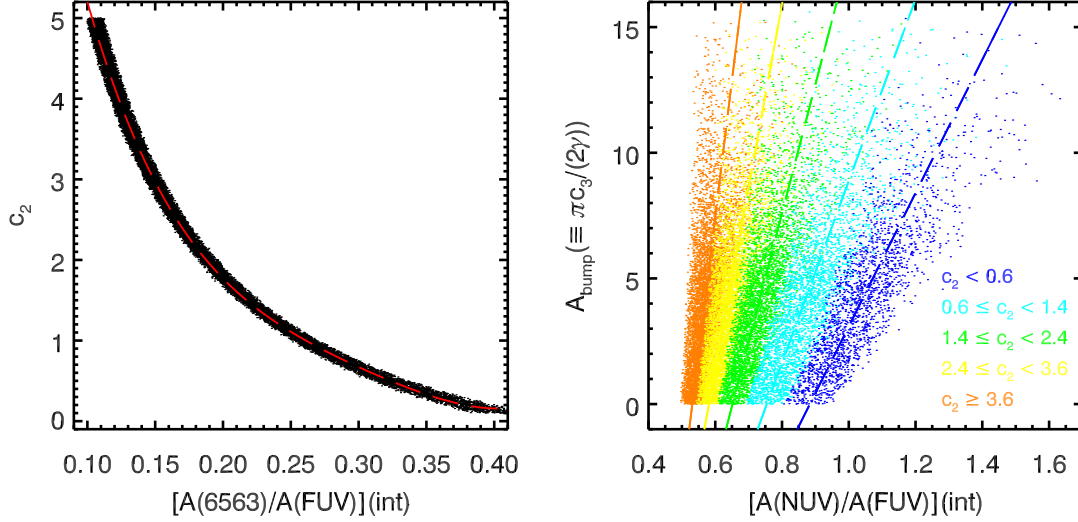


Figure 9. Left: c_2 vs. ratio of intrinsic 6563 Angstrom to FUV attenuations for the artificial sample described in Section 4, and the red dashed line is the best-fitting curve for the data, defined as Equation (7). Right: A_{bump} vs. ratio of intrinsic NUV to FUV attenuations for the same artificial sample, where the points in this panel are color-coded by c_2 : $c_2 < 0.6$ (blue), $0.6 \leq c_2 < 1.4$ (cyan), $1.4 \leq c_2 < 2.4$ (green), $2.4 \leq c_2 < 3.6$ (yellow), and $c_2 \geq 3.6$ (orange), and the dashed lines show the best-fitting curves for the subsamples with identical colors.

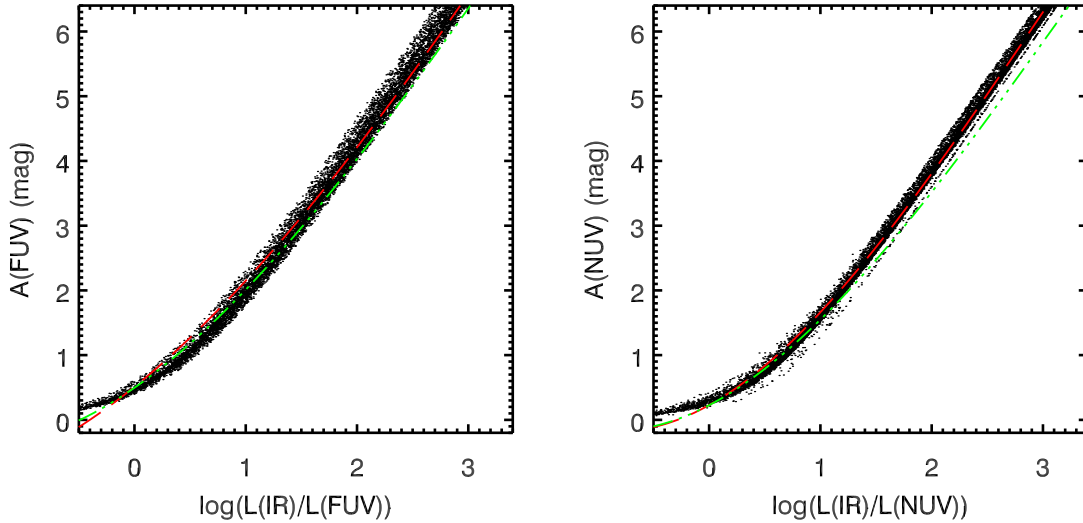


Figure 10. $A(\text{FUV})$ as a function of $\log(L(\text{IR})/L(\text{FUV}))$ in the left panel, and $A(\text{NUV})$ as a function of $\log(L(\text{IR})/L(\text{NUV}))$ in the right panel, for the artificial sample described in Section 4. In both panels, the red dashed lines are the best fitting curves for the data, and the green triple-dot-dashed lines show the B05 relations defined as Equations (4) and (5).

uum attenuation (i.e., $A(6563)$),¹⁸ for the sake of quantitative constraints on the parameters in the attenuation curve from observational properties.

Figure 9 shows c_2 as a function of $A(6563)/A(\text{FUV})$ and

¹⁸ With regard to the conversion $A(6563) = 0.44A(\text{H}\alpha)$ applied in this paper, we will discuss the uncertainties introduced by variations in the conversion factor from 0.44 in the results in Section 5.3.

A_{bump} as a function of $A(\text{NUV})/A(\text{FUV})$ for the artificial sample. In the left panel, $A(6563)/A(\text{FUV})$ correlates tightly with c_2 , demonstrating that $A(6563)/A(\text{FUV})$ is in a good position to trace the linear background slope. In the right panel, the dependence of $A(\text{NUV})/A(\text{FUV})$ on A_{bump} is almost invisible, but with a series of constant c_2 ranges assigned, the correlation between $A(\text{NUV})/A(\text{FUV})$, A_{bump} , and c_2 can be

obviously seen. This figure serves as a vivid description of the degeneracy between the linear background slope and the 2175 Angstrom bump in *GALEX* UV bands and at the same time manifests the validity of the combination of $A(\text{FUV})$, $A(\text{NUV})$, and $A(6563)$ in estimating c_2 and A_{bump} . In order to quantify the estimation of c_2 and A_{bump} from $A(\text{FUV})$, $A(\text{NUV})$, and $A(6563)$, we conduct polynomial fits for the two correlations. The best-fitting formulae are displayed as follows:

$$c_2 = 1263.35x_3^4 - 1555.11x_3^3 + 733.92x_3^2 - 164.59x_3 + 15.75, \quad (7)$$

and

$$A_{\text{bump}} = 0.73x_3^2x_4 - 100.78x_3x_4 + 56.19x_4 + 215.99x_3^2 - 86.42x_3 - 13.94, \quad (8)$$

where $x_3 \equiv A(6563)/A(\text{FUV})$ and $x_4 \equiv A(\text{NUV})/A(\text{FUV})$. Because of the upper and lower limits in the parameter ranges in the fitting, we suggest that Equations (7) and (8) are applicable to the data within the range of $0.1 \leq A(6563)/A(\text{FUV}) \leq 0.4$ and $0.4 \leq A(\text{NUV})/A(\text{FUV}) \leq 1.6$. Uncertainties in the estimates of c_2 and A_{bump} from $A(\text{FUV})$, $A(\text{NUV})$, and $A(6563)$ by adopting Equations (7) and (8) will be discussed in the paragraphs below.

In the previous section of this paper, $A(\text{FUV})$ and $A(\text{NUV})$ for the observational data are derived from $\log(L(\text{IR})/L(\text{FUV}))$ and $\log(L(\text{IR})/L(\text{NUV}))$, respectively, by using the B05 calibration, and then they are adopted to probe the features of the attenuation curve. In this situation, it is necessary to examine the reliability of the B05 calibration, i.e., whether or not the B05 calibration is independent of any presumption of the attenuation curve.

Our mock objects cover a wide variety of attenuation curves and therefore serve as an excellent sample for this examination. In Figure 10, we plot $A(\text{FUV})$ as a function of $\log(L(\text{IR})/L(\text{FUV}))$ and $A(\text{NUV})$ as a function of $\log(L(\text{IR})/L(\text{NUV}))$ for the artificial sample, and we also superimpose the best-fitting curves for our mock data as well as the B05 calibration curves on both diagrams for comparison purposes. The tight locus composed by the data points in each panel of this figure proves the IR-to-UV ratios to be intrinsically insensitive to the shapes of the attenuation curve. The best-fitting curves for the mock objects are formulated as the following equations:

$$A(\text{FUV}) = -0.0200x_1^3 + 0.2722x_1^2 + 1.3859x_1 + 0.5112, \quad (9)$$

and

$$A(\text{NUV}) = -0.0597x_2^3 + 0.5334x_2^2 + 0.9605x_2 + 0.2287, \quad (10)$$

where $x_1 \equiv \log(L(\text{IR})/L(\text{FUV}))$ and $x_2 \equiv \log(L(\text{IR})/L(\text{NUV}))$. The B05 calibration is in good agreement with our fitting in each panel of Figure 10. The maximum difference between the two calibrations is 0.25 mag in either $A(\text{FUV})$ or $A(\text{FUV}) - A(\text{NUV})$ for $-0.5 < \text{IRX} < 3.4$, and 0.04 in $A(\text{NUV})/A(\text{FUV})$ for $-0.2 < \text{IRX} < 3.4$, as shown in Figure 11. This examination implies that even if we change the formula during the estimation of FUV and NUV attenuations, there will not be any significant effect on the results; a remarkable disparity between the two calibrations occurs only when $\text{IRX} > 4.0$, which is beyond most observations. Consequently, the B05 calibration in general cases offers a reliable, unbiased diagnosis of the attenuation curve.

The artificial sample also helps to assess uncertainties in the prescription for constraints on the attenuation curve. In

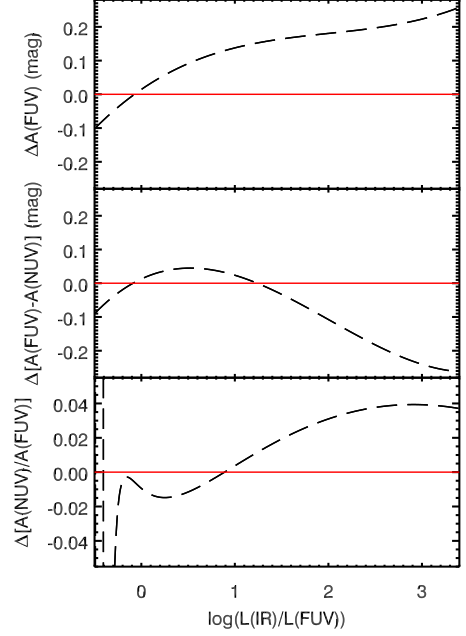


Figure 11. Top: margin between $A(\text{FUV})$ estimated with the calibrations in this work (red dashed line in Figure 10) and in B05 (green triple-dot-dashed line in Figure 10), as a function of $\log(L(\text{IR})/L(\text{FUV}))$. Bottom: margin between $A(\text{NUV})/A(\text{FUV})$ estimated with the calibrations in this work (red dashed line in Figure 10) and in B05 (green triple-dot-dashed line in Figure 10), as a function of $\log(L(\text{IR})/L(\text{FUV}))$.

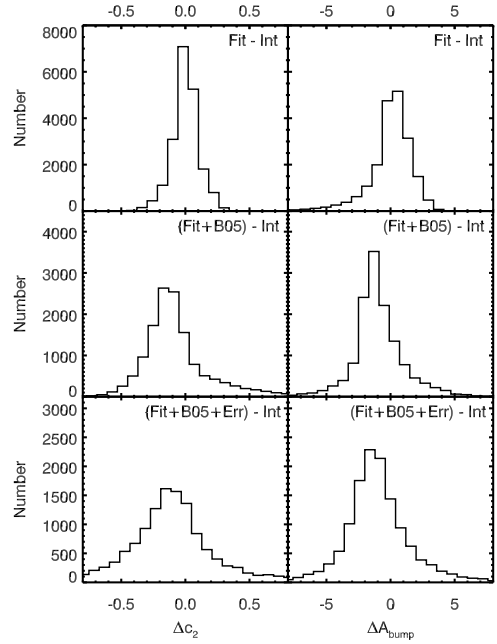


Figure 12. Histograms of Δc_2 (left column) and ΔA_{bump} (right column) for the artificial sample described in Section 4. Δc_2 and ΔA_{bump} are the differences in c_2 and A_{bump} between the estimated and intrinsic values described in Section 4.3. All the data in the mock catalog are plotted in the top row, while the data with $\text{IRX} \leq 4.0$ are shown in the middle and bottom rows.

the top panel of Figure 12, estimates of c_2 and A_{bump} from intrinsic $A(\text{FUV})$ and $A(\text{NUV})$ by adopting Equations (7) and (8) have a standard deviation of $\sim \pm 0.1$ in c_2 and $\sim \pm 1.7$ in A_{bump} . With the B05 calibration used to obtain $A(\text{FUV})$ and $A(\text{NUV})$ from $\log(L(\text{IR})/L(\text{FUV}))$ and $\log(L(\text{IR})/L(\text{NUV}))$

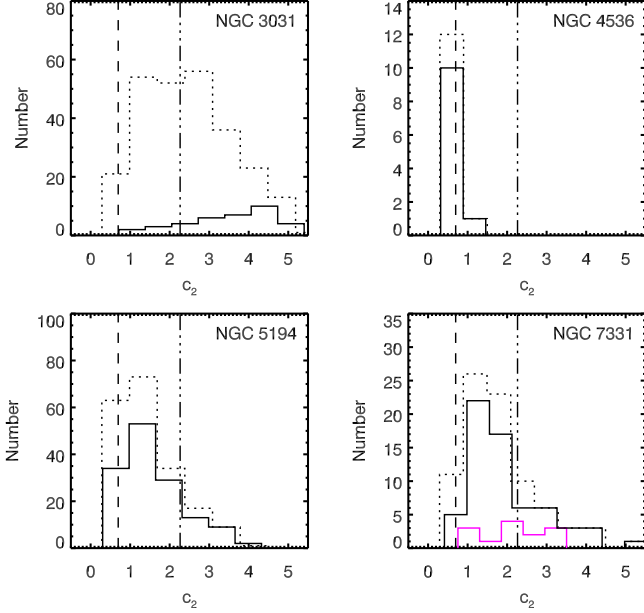


Figure 13. Histograms of c_2 for the UV and IR clusters inside NGC 3031 (top left panel), NGC 4536 (top right panel), NGC 5194 (bottom left panel), and NGC 7331 (bottom right panel), estimated by adopting Equation (7). In each panel, the solid line describes the clusters with $\text{IRX} > 0.6$, while the dotted line shows all the clusters measured in the galaxy; specifically for NGC 7331, the black lines represent the disk clusters, and the magenta line represents the ring clusters. The dashed line marks the value of the MW c_2 , and the triple-dot-dashed line marks the value of the SMC c_2 .

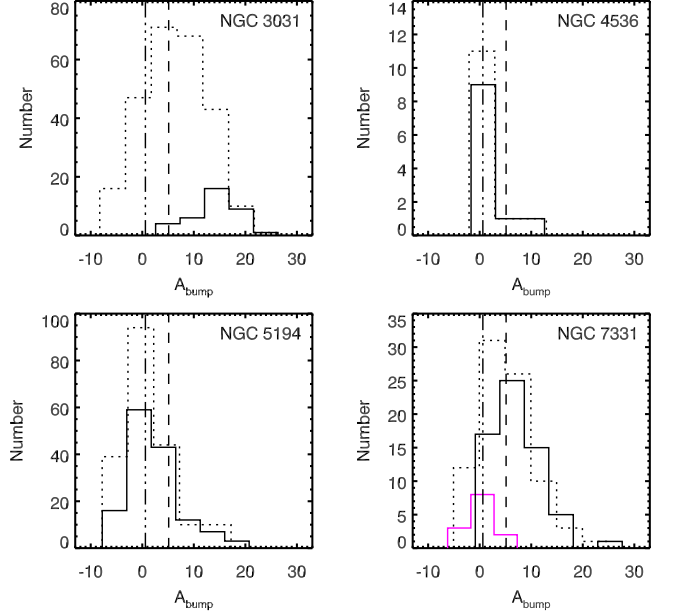


Figure 14. Histograms of A_{bump} for the UV and IR clusters inside NGC 3031 (top left panel), NGC 4536 (top right panel), NGC 5194 (bottom left panel), and NGC 7331 (bottom right panel) estimated by adopting Equation (8). In each panel, the solid line describes the clusters with $\text{IRX} > 0.6$, while the dotted line shows all the clusters measured in the galaxy; specifically for NGC 7331, the black lines represent the disk clusters, and the magenta line represents the ring clusters. The dashed line marks the value of the MW A_{bump} , and the triple-dot-dashed line marks the value of the SMC A_{bump} .

but without photometric uncertainties imposed on the quantities, the application of Equations (7) and (8) introduces a slight offset of ~ -0.1 in c_2 and ~ -1.2 in A_{bump} and a standard deviation of $\sim \pm 0.3$ in c_2 and $\sim \pm 2.2$ in A_{bump} , which can be seen from the middle panels of this figure.¹⁹ After adding the simulated photometric uncertainties to the mock data, Equations (7) and (8) in combination with the B05 formula result in the same level of offset and the standard deviation of $\sim \pm 0.5$ in c_2 and $\sim \pm 2.8$ in A_{bump} , as shown in the bottom panels in Figure 12. This examination reflects that uncertainties introduced by calibration and photometry are likely to deviate the estimates of the parameters in the attenuation curve from the intrinsic values at a certain degree, but effective constraints can still be made with the uncertainties taken into account and are able to at least distinguish between the MW- and SMC-type signatures.

In addition to the B05 formula, Burgarella et al. (2005) offers similar formulae to estimate $A(\text{FUV})$ and $A(\text{NUV})$ from $\log(L(\text{IR})/L(\text{FUV}))$ and $\log(L(\text{IR})/L(\text{NUV}))$. By comparing this calibration with the B05 formula, we find very trivial differences between the results, with a mean value of < 0.03 mag in $A(\text{FUV})$ and ~ 0.05 mag in $A(\text{FUV}) - A(\text{NUV})$. Also, there are several other formulae for the conversion from $\log(L(\text{IR})/L(\text{FUV}))$ to $A(\text{FUV})$ (e.g., Meurer et al. 1999; Kong et al. 2004; Hao et al. 2011; Boquien et al. 2012). As discussed elaborately in Hao et al. (2011); Boquien et al. (2012), these various estimates of $A(\text{FUV})$, including those with the B05 calibration, are very close to each other, but

¹⁹ In the middle and bottom panels of Figure 12, we do not plot the data in the artificial sample with $\text{IRX} > 4.0$, in order to avoid the additional error resulting from the application of the B05 formula to $\text{IRX} > 4.0$, as mentioned in the above paragraph.

in most of the formulas, the estimate of $A(\text{NUV})$ requires a presumption of a certain type of attenuation curve. In this case, the combination of $A(\text{FUV})$ and $A(\text{NUV})$ is inherently biased and therefore fails to trace the features of the attenuation curve. Because of this factor, we employ the B05 formula, which separately calibrates $A(\text{FUV})$ and $A(\text{NUV})$ in our work.

With the application of Equations (7) and (8) to the clusters (with $0.1 \leq 0.44A(\text{H}\alpha)/A(\text{FUV}) \leq 0.4$, and $0.4 \leq A(\text{NUV})/A(\text{FUV}) \leq 1.6$) inside NGC 3031, NGC 4536, NGC 5194, and NGC 7331, we estimate c_2 and A_{bump} from $A(\text{FUV})$, $A(\text{NUV})$, and $A(\text{H}\alpha)$ for these galaxies. Figures 13 and 14 show the histograms of the derived c_2 and A_{bump} for each of the galaxies, where we plot the clusters with $\text{IRX} > 0.6$ as the solid line and a total number of the clusters as the dotted line, since the estimates of c_2 and A_{bump} for objects with $\text{IRX} < 0.6$ are potentially influenced by variations in stellar population age, which will be discussed in Section 5.2.

In Figures 13 and 14, taking the total number of the clusters into account, NGC 3031 presents the linear background slope spanning over a broad range with a typical value of about 2.2 in c_2 , comparable to the SMC slope, and the 2175 Angstrom bump stronger than the MW type with $A_{\text{bump}} > 5.0$ for a majority of the clusters. On the contrary, the attenuation curve for NGC 4536 appears with shallow and bumpless features ($c_2 \sim 0.6$ and $A_{\text{bump}} \sim 0.0$) and can be characterized by the MW-type linear background but with no bump.²⁰ The similar bumpless feature is displayed in NGC 5194, with the mod-

²⁰ Due to the criterion of $0.1 \leq 0.44A(\text{H}\alpha)/A(\text{FUV}) \leq 0.4$, a number of the clusters with high $\text{H}\alpha$ attenuation inside NGC 4536 are excluded in the estimation of c_2 and A_{bump} .

erate linear background ranging between the MW- and the SMC-type slopes with a typical value of $c_2 \sim 1.3$ suggested in the attenuation curve. For NGC 7331, most of the disk clusters inside NGC 7331 present a moderate linear background slope comparable to that for NGC 5194 and a 2175 Angstrom bump as strong as the MW-type bump with $A_{\text{bump}} \sim 5.0$ on average; the ring clusters cover a wide range in the linear background slope but appear to have a very trivial or even absent bump in the attenuation curve, similar to those for NGC 4536 and NGC 5194. The classification of the clusters with $\text{IRX} > 0.6$ does not lead to any obvious difference in the results except for NGC 3031 where only a small percentage of the clusters have $\text{IRX} > 0.6$ in contrast to the other galaxies. Compared with the majority of clusters in NGC 3031, the clusters with $\text{IRX} > 0.6$ are exhibited to have a steeper linear background and a stronger 2175 Angstrom bump.

Although Equations (7) and (8) offer a prescription for quantitative constraints on the parameters in the attenuation curve, the combination of $A(\text{FUV})$, $A(\text{NUV})$, and $A(\text{H}\alpha)$ remains to be a rough tracer. In any case, more accurate estimates of the attenuation curve are based on the analysis of the spectral continuum taken from spectroscopic observations.

5. DISCUSSION

Ever since the deviation in the IRX-UV relation was initially found in observations of galaxies, a number of studies – from the interpretation offered by Kong et al. (2004) a decade ago to the very recent research taken by Grasha et al. (2013) – have suggested stellar population age to be the second parameter in the IRX-UV function. Through a census of the impacts of various physical parameters on the IRX-UV relation conducted by the SED fitting technique, Boquien et al. (2012) have suggested that, in addition to the intrinsic UV color of a stellar population being found to primarily determine the IRX-UV distribution for galaxies, a secondary but non-negligible role is played by the shape of the attenuation curve. The above sections in this paper present the influences of the attenuation curve on the IRX-UV relation; however, until now there has not been any successful observation of the features of the attenuation curve in the IRX-UV relation. As we have analyzed in the above section, the degeneracy of the linear background slope and the 2175 Angstrom bump strength in UV wavelength bands is likely to be one significant obstacle. In this section, we will discuss other possible reasons for the failure in observational measurements of the parameters related to the attenuation curve in the IRX-UV function.

5.1. Age Effects on the IRX-UV Relation

As Boquien et al. (2012) have pointed out, variations in intrinsic UV color are the main cause of the deviation in the IRX-UV relation. In most cases, stellar population age, compared with other physical parameters such as initial mass function and metallicity, dominates intrinsic UV color more effectively. In Paper I, we have investigated the influences of stellar population age on the IRX-UV relation, which appear to be a considerable offset toward redder UV colors for older stellar populations but appear to be gradually invisible as the star formation timescale increases. The maximum effect of stellar population age exists in simple stellar populations with the SFH of an instantaneous burst or a short star formation timescale (e.g., $\tau_{\text{SF}} \leq 0.01$ Gyr). In this kind of SFH scenario, as shown in Figure 16 in Paper I as an example, the intrinsic UV color for a 100 Myr stellar population is

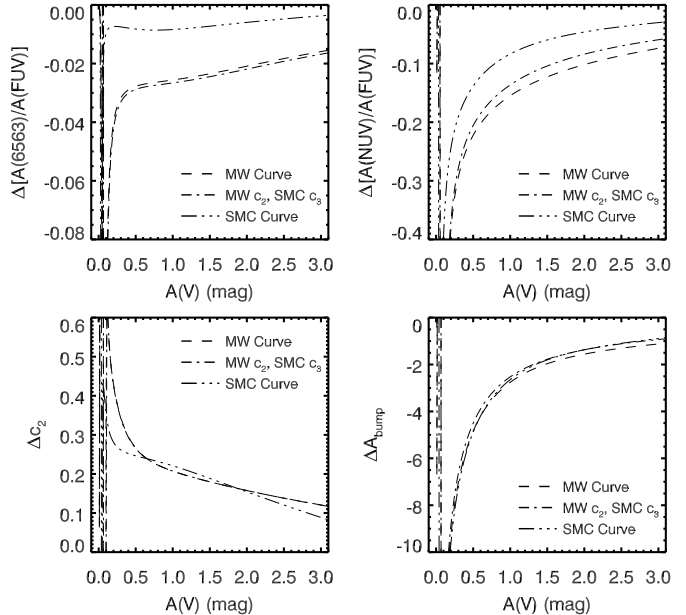


Figure 15. Differences between 2 and 100 Myr stellar populations in $A(6563)/A(\text{FUV})$ (top left panel), $A(\text{NUV})/A(\text{FUV})$ (top right panel), c_2 (bottom left panel), and A_{bump} (bottom right panel) as a function of $A(V)$. The lines in each panel are obtained by spectral synthesis modeling with different attenuation curves: the MW curve (dashed line), the M-S curve (dot-dashed line), and the SMC curve (triple-dot-dashed line), which is described in Section 2. $A(\text{FUV})$ and $A(\text{NUV})$ are derived from $\log(L(\text{IR})/L(\text{FUV}))$ and $\log(L(\text{IR})/L(\text{NUV}))$ by using Equations (4) and (5), and c_2 and A_{bump} are derived from the combination of $A(\text{FUV})$, $A(\text{NUV})$, and $A(6563)$ by using Equations (7) and (8).

redder than that for a 2 Myr stellar population by a factor of ~ 0.5 mag in FUV – NUV; as stellar populations continue to evolve, the offset in intrinsic UV color from the 2 Myr stellar population extends more intensively, for instance, to ~ 2.0 mag for a 500 Myr stellar population and to ~ 4.0 mag for a 1 Gyr stellar population. Even though more complex SFHs give birth to composite stellar populations and thus complicate the correlation between stellar population age and intrinsic UV color, there is no doubt that age effects substantially deviate the IRX-UV relation, particularly for systems containing evolved stellar populations.

In this paper, as can be seen from the right panel of Figure 3, the difference between FUV – NUV produced by the MW- and SMC-type attenuation curves for the same stellar population age (i.e., with the same intrinsic UV color) increases with rising IRX, for instance, to ~ 0.5 mag at $\text{IRX} \sim 0.5$ and to ~ 2.0 mag at $\text{IRX} \sim 2.5$. By combining the results in Paper I and those in this paper, we can imply that because of the age effects that seriously vary intrinsic UV color, the role played by the attenuation law in the IRX-UV relation is possibly obscured and therefore difficult to detect even though variations in the attenuation curve still introduce uncertainties into observational properties for galaxies. In this situation, the features of the attenuation law are distinguishable only for young (approximately < 100 Myr) and dust-rich (at least $\text{IRX} > 0.5$) stellar populations; otherwise, stellar population age tends to have a predominant influence on the IRX-UV relation, as Grasha et al. (2013) have confirmed by compiling and investigating a sample of galaxies with the stellar population age in the range of 10 Myr–5 Gyr and $\text{IRX} \leq 0.5$.

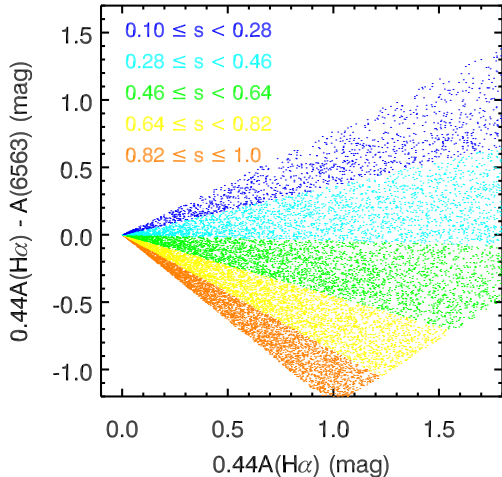


Figure 16. Residuals between $0.44A(\text{H}\alpha)$ and $A(6563)$ as a function of $0.44A(\text{H}\alpha)$ for the artificial sample described in Section 5.3, where $0.44A(\text{H}\alpha) = 0.44A(6563)/s$. The points are color-coded by the conversion factor s : $0.30 \leq s < 0.34$ (blue), $0.34 \leq s < 0.38$ (cyan), $0.38 \leq s < 0.42$ (green), $0.42 \leq s < 0.46$ (yellow), and $0.46 \leq s < 0.50$ (orange).

5.2. Requirement for Dust Content in the Diagnostics of the Attenuation Law

Accurate measurements of the parameters related to the attenuation curve are always a challenge. Without available spectral observations, a comparison between attenuations at different wavelength bands appears to be a feasible approach. In this paper, we adopt FUV, NUV, and 6563 Angstrom attenuations to probe the linear background and the 2175 Angstrom bump in the attenuation curve. The estimation of FUV and NUV attenuations is based on the B05 formula (Equations (4) and (5) deriving $A(\text{FUV})$ and $A(\text{NUV})$ from $\log(L(\text{IR})/L(\text{FUV}))$ and $\log(L(\text{IR})/L(\text{NUV}))$, respectively. However, as Cortese et al. (2008) have suggested, the correlation between $A(\text{UV})$ and $\log(L(\text{IR})/L(\text{UV}))$ is also biased by the stellar population age. Fortunately, the sample studied in our work contains only young clusters inside galaxies, and from the modeled lines in Figure 4 we can see that $\log(L(\text{IR})/L(\text{FUV}))$ varies by a factor of < 0.2 for the same amount of attenuation as long as stellar populations are younger than 100 Myr. Nevertheless, although this variation is too trivial to introduce deviation into the IRX-UV relation, the features of the attenuation curve probed by comparing attenuations at different bands are still unable to withstand age or/and other effects if dust content is low.

In order to explore the requirement for dust content in the diagnostics of the attenuation curve, we examine the systematic uncertainties in $A(6563)/A(\text{FUV})$, $A(\text{NUV})/A(\text{FUV})$, c_2 , and A_{bump} induced by the difference between 2 and 100 Myr stellar population ages for the three typical attenuation curves, the MW curve, the M-S curve, and the SMC curve, as a function of $A(V)$, on the basis of the stellar population synthesis modeling described in Section 2. In this examination, $A(\text{FUV})$ and $A(\text{NUV})$ are derived from $\log(L(\text{IR})/L(\text{FUV}))$ and $\log(L(\text{IR})/L(\text{NUV}))$ by using Equations (4) and (5), and c_2 and A_{bump} are derived from the combination of $A(\text{FUV})$, $A(\text{NUV})$, and $A(6563)$ by using Equations (7) and (8). The results are shown in Figure 15, where the difference in each of the compared quantities between 2 and 100 Myr stellar populations ($[100 \text{ Myr}] - [2 \text{ Myr}]$) appears to increase with declin-

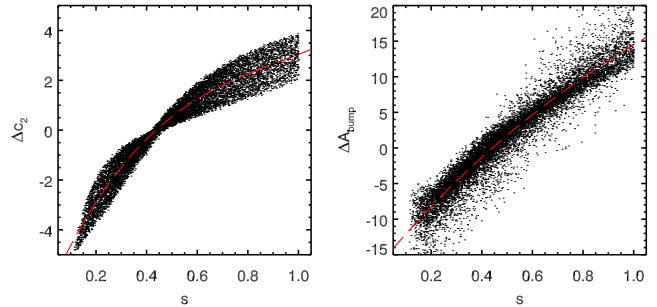


Figure 17. Δc_2 (left panel) and ΔA_{bump} (right panel) as a function of the conversion factor s for the artificial sample described in Section 5.3, where Δc_2 and ΔA_{bump} are the differences of the estimates by using Equations (7) and (8) with various s from intrinsic c_2 and A_{bump} . The red dashed lines superimposed on the left and the right panels are the best-fitting curves for the data, defined as Equations (12) and (13), respectively.

ing $A(V)$. This trend implies that variations in stellar population age have more potential to seriously affect the estimates of the attenuation curve for systems with lower dust content albeit stellar populations younger than 100 Myr. In particular, when $A(V) < 0.5$, if we estimate the linear background slope and the 2175 Angstrom bump strength for objects with the same attenuation curve but ranging from 2 Myr to 100 Myr, the maximal difference in the results is likely to exceed 0.25 in c_2 and 4.5 in A_{bump} . As also displayed in this figure, random errors become tremendous when $A(V) < 0.08$, and in this case it is impossible to give any reliable estimate.

The requirement for dust-rich systems tends to be another difficulty in tracing the parameters related to the attenuation curve and hampers our attempt to acquire explicit information about the attenuation curve for galaxies or clusters with low dust content. With this in mind, we solidify the data with $\text{IRX} > 0.6$ (which approximately fulfill $A(V) > 0.5$) in Figures 13 and 14, and plot the entire sample by dotted lines for distinction, although for our sample there is no obvious disparity in the results except for NGC 3031, where most of the clusters lie at low attenuation levels.

5.3. Variations in Conversion Factor between $A(\text{H}\alpha)$ and $A(6563)$

In this paper, we employ $A(6563)$ in combination with $A(\text{FUV})$ and $A(\text{NUV})$ to break the degeneracy of the linear background and the 2175 Angstrom bump in UV wavelength bands. The $A(6563)$ for observational data is translated from $A(\text{H}\alpha)$ by adopting the conversion $A(6563) = 0.44A(\text{H}\alpha)$ calibrated in Calzetti (1997). However, the conversion factor between $A(\text{H}\alpha)$ and $A(6563)$ is considered to depend on the geometric configuration between dust, gas, and stars and to vary in different environments. The assumption of the fixed value 0.44 is an empirical simplification and likely to introduce an extra uncertainty into the results. In this subsection, we make an examination of this potential influence on the results.

By denoting the conversion factor as s , the conversion becomes

$$A(6563) = sA(\text{H}\alpha). \quad (11)$$

According to this definition, the assumption of the fixed value 0.44 for the factor s yields the transform of $0.44A(\text{H}\alpha) = 0.44A(6563)/s$, where $0.44A(\text{H}\alpha)$ is the derived $\text{H}\alpha$ -band continuum attenuation and $A(6563)$ is the intrinsic $\text{H}\alpha$ -band continuum attenuation

The difference between $0.44A(\text{H}\alpha)$ and $A(6563)$ as a function of $0.44A(\text{H}\alpha)$ is illustrated in Figure 16 for the artificial sample described in Section 4, where s varies in the range of 0.1–1.0. It is obvious to see that in the case of variable s , there is likely to be considerable deviation in the estimates of $\text{H}\alpha$ -band continuum attenuation by assuming $s = 0.44$. For instance, if we obtain $0.44A(\text{H}\alpha) = 1.0$ mag, a variation of ± 0.1 in s will deviate the result by about ± 0.2 mag, and a variation of ± 0.2 in s will increase the deviation to about ± 0.5 mag.

Figure 17 shows the deviation in c_2 and A_{bump} as a function of s , respectively, for the artificial sample. We also formulate the influences of the variable s on c_2 and A_{bump} via polynomial fits. The best-fitting curves are superimposed on Figure 17, and the equations are presented as follows:

$$\Delta c_2 = 7.42s^3 - 20.67s^2 + 23.03s - 6.74, \quad (12)$$

and

$$\Delta A_{\text{bump}} = 3.17s^3 - 15.34s^2 + 42.86s - 16.23. \quad (13)$$

Apparently, if the variations in the factor s exceed a certain range, it will have a remarkable impact on the derivation of the linear background slope and the 2175 Angstrom bump area from $A(\text{H}\alpha)$. For instance, a variation of ± 0.1 in s around 0.44 introduces uncertainties of about -1.0 to 0.8 in c_2 and about -3.3 to 2.9 in A_{bump} , and a variation of ± 0.2 in s around 0.44 increases the uncertainties to about -2.3 to 1.5 in c_2 and about -6.8 to 5.7 in A_{bump} .

Let us take NGC 3031 and NGC 7331 as an example to describe the influences in two extreme cases. In the previous sections, with $s = 0.44$, we have suggested the presence of a prominent bump for NGC 3031 and a bumpless feature for the central ring in NGC 7331. However, for NGC 3031, if the intrinsic value of the factor is $s = 0.64$, then the result from the assumption of $s = 0.44$ would overestimate A_{bump} by about 5.7, and in this case, NGC 3031 appears with a bumpless feature and a very shallow slope. For the NGC 7331 central ring, if the intrinsic value of the factor is $s = 0.24$, then the result from the assumption of $s = 0.44$ would underestimate A_{bump} by about 6.8, and in this case, the ring area has a strong bump in the attenuation curve with a much steeper slope.

A strict calibration of the conversion factor s requires separate estimates of $A(\text{H}\alpha)$ and $A(6563)$ from observations. At present, alternative values have been suggested in several studies (Babbedge et al. 2005; Argence & Lamareille 2009), and as a specific example, with a combination of photometrical SED fitting and spectral emission-line diagnostics, Lin et al. (2013) find the best-fitting value of $s \sim 0.32$ for star-forming regions inside a nearby spiral galaxy M101. The geometric configuration between dust, gas, and stars is suspected to dominate this conversion factor. According to the age-selective attenuation, younger stellar populations tend to encounter heavier attenuation (i.e., $A(6563)$ varies with stellar population age. Granato et al. 2000; Panuzzo et al. 2007), and in this case if we assume a constant geometry between dust and gas in different environments (i.e., $A(\text{H}\alpha)$ is constant), then the value of s will decrease as stellar populations evolve. This scenario can be roughly applied to galaxies as a whole. For subregions in galaxies, the actual geometries seem to be more complicated, and the influences on local geometries between dust, gas, and stars include particle interaction and dynamics, radiative fields, stellar winds and shocks, etc. Separate probes into gas and stars are necessary to recalibrate

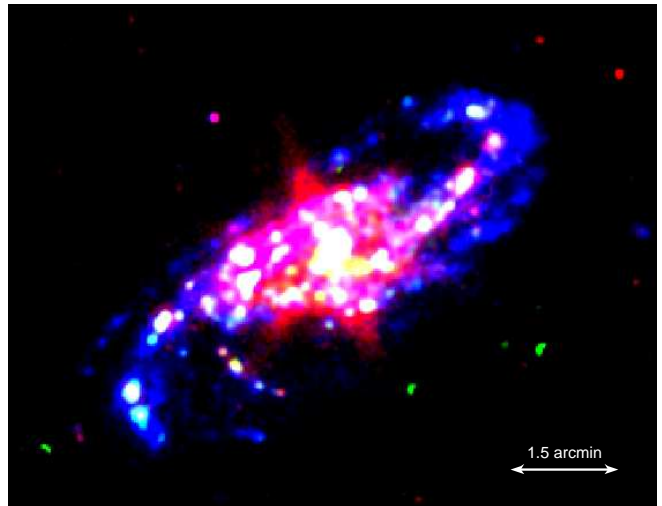


Figure 18. Three-color composite image of NGC 4536. The FUV (blue), continuum-subtracted $\text{H}\alpha$ (green) and $24 \mu\text{m}$ (red) images are retrieved from GALEX, a ground-based telescope, and *Spitzer* observations respectively. The scale in the bottom right corner indicates the $1'.5$ length. North is up and east is to the left.

this conversion.

5.4. $\text{H}\alpha$ Attenuation for NGC 4536

As we have mentioned in Section 3.3, a majority of the clusters inside NGC 4536 except the galactic core, appear with a larger amount of $\text{H}\alpha$ -band continuum attenuation than the expectation from the MW curve, hinting at shallower slopes than the MW type for these regions (shown in the top left panel of Figure 6). However, this phenomenon conflicts with the $A(\text{FUV})$ versus $A(\text{FUV}) - A(\text{NUV})$ diagram for this galaxy (the top left panel of Figure 5) that requires the MW-type or steeper slopes, otherwise it will have to yield a negative bump (i.e., a trough) in the attenuation curve. The discussion in the above subsection implies that if the conversion factor s differs from the assumed value 0.44, the observed relation between $A(\text{FUV})$ and $0.44A(\text{H}\alpha)$ would be influenced. In consideration of this effect, we find that, when the factor s is adjusted to ~ 0.25 – 0.3 , most of the data points from NGC 4536 are able to fit the MW slope. As a result, the variations in s provide a tentative explanation of the discrepancy between the diagrams in Figures 5 and 6 for NGC 4536.

Notwithstanding, there is another possible reason for this $A(\text{H}\alpha)$ conundrum, which rests in the mismatch between $24 \mu\text{m}$ and $\text{H}\alpha$ emission from NGC 4536. In this work, $A(\text{H}\alpha)$ is derived from the ratio of $24 \mu\text{m}$ to $\text{H}\alpha$ luminosities by using Equation (6). As we have introduced in Section 3.3, the application of Equation (6) avails on the basis of the correlation between $24 \mu\text{m}$ and intrinsic $\text{H}\alpha$ luminosities for star-forming regions (i.e., a constant value for $24 \mu\text{m}$ -to- $\text{H}\alpha$ in unattenuated environments). However, the measured $24 \mu\text{m}$ luminosities for the vast majority of the clusters inside NGC 4536 are suspected to exceed the local star-forming properties. Figure 18 shows a composite image of FUV, continuum-subtracted $\text{H}\alpha$, and $24 \mu\text{m}$ emission for NGC 4536. In this image, the FUV pattern exhibits a clear spiral structure, and the $\text{H}\alpha$ knots reside along the spiral arms. The most conspicuous appearance of this galaxy in this figure is a giant $24 \mu\text{m}$ -emitting clump covering from the center to over half of the galactic radius. The intensive central star-forming activities performed in NGC 4536 (Jogee et al. 2005) are considered as the energy

source to heat interstellar dust on this large scale and contribute the prominent IR emission. In contrast to this $24\ \mu\text{m}$ property, there is no compatible $\text{H}\alpha$ source inside this galaxy, and the central star formation is only able to ionize limited regions of gas. As a consequence, most of local $24\ \mu\text{m}$ sources inside NGC 4536 are likely to be contaminated from the central emission, which potentially induces an overestimate of $24\ \mu\text{m}$ luminosities in photometry for the local star-forming properties linked to the $\text{H}\alpha$ emission (i.e., a larger value for the ratio of $24\ \mu\text{m}$ to intrinsic $\text{H}\alpha$ luminosities). In such a case, Equation (6) with the assumption of $a = 0.031$ is suspected to overestimate the $\text{H}\alpha$ attenuation, and as a consequence, a majority of the data points from NGC 4536 present higher $A(\text{H}\alpha)$ at fixed $A(\text{FUV})$ than any model expectation in Figure 6, resulting in shallower slopes in the attenuation curve. Nevertheless, the $24\ \mu\text{m}$ excess does not take place in the core of this galaxy where the $24\ \mu\text{m}$ and the $\text{H}\alpha$ luminosities are related to the same energy source, and the location of the central clusters in Figure 6 is well fitted by the MW-type slope.

6. SUMMARY AND OUTLOOK

The main purpose of this work is to investigate the features of the attenuation law on both a theoretical and observational basis and thus to offer a complementary interpretation of the dispersion in the IRX-UV relation as a continuation of Paper I, which has discovered the influences of stellar population age.

In this paper, the spectral synthesis modeling predicts the linear background and the 2175 Angstrom bump in the attenuation curve to be two additional parameters in the IRX-UV function; at the same time, the spatially resolved study of the four nearby galaxies, NGC 3031, NGC 4536, NGC 5194, and NGC 7331, provides an observational insight into the features of the attenuation curve.

The linear background with steeper slope, as thoroughly examined in our work, is responsible for redder UV color; the 2175 Angstrom bump, however, tends to diminish the reddening or even have a blueing impact on UV color if it is strong enough. By combining dust attenuations at the three different bands, FUV, NUV, and $\text{H}\alpha$, the linear background slope and the 2175 Angstrom bump for the four galaxies are estimated. In the results, NGC 3031 appears with a bump feature in the attenuation curve, but the lack of high attenuation data for this galaxy hinders more accurate constraints. NGC 4536 is well characterized by a bumpless attenuation curve with a MW-type slope similar to the C00 curve in shape. NGC 5194 also presents a bumpless feature in the attenuation curve but with the steeper slope between the MW and SMC types. NGC 7331 exhibits different features in the attenuation curve between the disk and the ring areas, where the disk regions are suggested to have the MW-type bump, and the ring regions manifest an evident absence of a bump in the attenuation curve. The variations in the attenuation curve interpret the deviation in the IRX-UV relation in an additional way and complement the scenarios assuming a constant attenuation curve addressed in Paper I. Our results for NGC 3031 and NGC 5194 are in agreement with earlier studies: Hoversten et al. (2011) have revealed the presence of a MW-type bump in the best-fitting attenuation curves for subregions inside NGC 3031, and Calzetti et al. (2005) have suggested a quite trivial property of the 2175 Angstrom bump in the attenuation curve for NGC 5194 in contrast to that for the MW.

People have been investigating the deviation in the correlation between the IR-to-UV ratio and the UV color (or UV spectral slope) for a long period of time, yet the features of the attenuation law have not been evidently discovered in observations. In this paper, several possible obstacles that prevent successful discoveries are discussed. The degeneracy of the linear background and the 2175 Angstrom bump in UV wavelength bands is suspected to be one significant cause and makes it impossible to distinguish between the features of the linear background and the 2175 Angstrom bump without suitable observations at other wavelength bands.

Before making efforts to probe and distinguish the parameters in the attenuation curve, people are usually perplexed with variations in intrinsic UV color for different galaxies in more general cases. The aging of stellar populations is a primary cause of the variation in intrinsic UV colors of galaxies and therefore dominates the scatter in the IRX-UV plane, as suggested in a number of papers (e.g., Kong et al. 2004; Dale et al. 2007, 2009; Boquien et al. 2012; Grasha et al. 2013) and especially characterized in Paper I. Because of the effects of stellar population age on intrinsic UV color, variations in the attenuation law become a subordinate origin of the deviation in the IRX-UV relation, particularly for composite stellar populations; moreover, even if a sample consists of stellar populations young enough with similar intrinsic UV colors, the features of the attenuation law are expected to be observable only for the dust-rich objects contained therein, since low dust content is still likely to leave the features masked by other effects.

A comparison of attenuations at different wavelength bands is a feasible approach to constraints on the attenuation curve. However, uncertainties in estimates of the attenuations have considerable potential to become an extra obstacle to probing the attenuation law. As a specific example, in this paper, during the estimation of $\text{H}\alpha$ -band continuum attenuation ($A(6563)$) from $\text{H}\alpha$ emission-line attenuation ($A(\text{H}\alpha)$), we assume the conversion factor of 0.44 as calibrated in Calzetti (1997). If this factor in reality happens to be different from 0.44, the resulting $A(6563)$ and the consequent diagnosis of the attenuation curve can be seriously affected, depending on the deviation between the assumed and real values as we have examined and discussed comprehensively in this paper.

Although the attenuation curve is suspected to vary in different galaxies, the connection between the attenuation curve and galaxy type has not been found with robust evidence. In our work, except for NGC 7331 where the central ring area presents a distinct feature from the disk, there is no evident correlation of the parameters in the attenuation curve with spatial locations discovered in other galaxies. At present, physical origins of the linear background and the 2175 Angstrom bump in the attenuation curve remain controversial, and most conclusions about this topic are drawn from experimental products in laboratory or theoretical work by modeling. The linear background appears to correlate with the size distribution of overall dust grains, and in particular small grains with sizes of $\sim 0.01\ \mu\text{m}$ are likely to contribute a remarkable rise in the slope (Desert et al. 1990; Li & Draine 2001; Zubko et al. 2004; Weingartner & Draine 2001; Clayton et al. 2003). The 2175 Angstrom bump is possibly produced by carbonaceous particles, since the $\pi \rightarrow \pi^*$ transition of electrons in carbonaceous molecules triggers the absorption of photons around 2175 Angstrom. Candidates of the bump carrier include amorphous carbon (Gadallah et al. 2011), Bucky Onion (Ruiz et al.

2005), graphite (Papoular & Papoular 2009), and polycyclic aromatic hydrocarbon (Joblin et al. 1992; Mallocci et al. 2004; Duley 2006; Steglich et al. 2011).

In addition to the physical origins, the geometric configuration between dust and stars is also able to effectively influence the shape of the attenuation curve. It is widely suggested that dust-star geometries are variable in different radiative field environments, which changes both the linear background and the 2175 Angstrom bump in the attenuation curve (e.g., Witt & Gordon 2000; Gordon et al. 2000; Calzetti 2001; Inoue et al. 2006; Panuzzo et al. 2007). The geometrical effects tend to prevail in measurements of not only galaxies as a whole, but also subregions on several hundreds or tens of parsec scale inside galaxies. In following studies of this series, we plan to investigate the physical and geometrical reasons for the variations in the attenuation law and to attempt to disclose the nature of different features in attenuation curve.

We are grateful to the anonymous referee for the careful review and instructive comments that have substantially improved the paper. We thank Robert C. Kennicutt Jr. for the initial discussion with us that helped to draw the general profile of this paper. This work is supported by the National Basic Research Program of China (973 program 2013CB834900), the National Natural Science Foundation of China (NSFC, Nos. 11225315 and 11320101002), the Specialized Research Fund for the Doctoral Program of Higher Education (SRFDP, No. 20123402110037), and the Strategic Priority Research Program "The Emergence of Cosmological Structures" of the Chinese Academy of Sciences (No. XDB09000000). Ye-Wei Mao acknowledges the support of the China Scholarship Council. This research has made use of the NASA/IPAC Extragalactic Database (NED), which is operated by the Jet Propulsion Laboratory, California Institute of Technology, under contract with the National Aeronautics and Space Administration. This research has also made use of the NASA Astrophysics Data System.

REFERENCES

- Aniano, G., Draine, B. T., Gordon, K. D., & Sandstrom, K. 2011, *PASP*, 123, 1218
- Argence, B., & Lamareille, F. 2009, *A&A*, 495, 759
- Babbedge, T. S. R., Whitaker, R., & Morris, S. 2005, *MNRAS*, 361, 437
- Bell, E. F. 2002, *ApJ*, 577, 150
- Bertin, E., & Arnouts, S. 1996, *A&AS*, 117, 393
- Bertin, E., Mellier, Y., Radovich, M., et al. 2002, *Astronomical Data Analysis Software and Systems XI*, 281, 228
- Bianchi, L., Clayton, G. C., Bohlin, R. C., Hutchings, J. B., & Massey, P. 1996, *ApJ*, 471, 203
- Bianchi, L., Madore, B., Thilker, D., et al. 2003, *The Local Group as an Astrophysical Laboratory*, eds. M. Livio & T. M. Brown, 10
- Boquien, M., Calzetti, D., Kennicutt, R., et al. 2009, *ApJ*, 706, 553
- Boquien, M., Buat, V., Boselli, A., et al. 2012, *A&A*, 539, A145
- Bouwens, R. J., Illingworth, G. D., Franx, M., et al. 2009, *ApJ*, 705, 936
- Bresolin, F., Garnett, D. R., & Kennicutt, R. C., Jr. 2004, *ApJ*, 615, 228
- Buat, V., Iglesias-Páramo, J., Seibert, M., et al. 2005, *ApJ*, 619, L51
- Buat, V., Giovannoli, E., Heinis, S., et al. 2011, *A&A*, 533, A93
- Buat, V., Noll, S., Burgarella, D., et al. 2012, *A&A*, 545, A141
- Buat, V., & Xu, C. 1996, *A&A*, 306, 61
- Burgarella, D., Buat, V., & Iglesias-Páramo, J. 2005, *MNRAS*, 360, 1413
- Calzetti, D. 1997, *The Ultraviolet Universe at Low and High Redshift: Probing the Progress of Galaxy Evolution*, AIP Conference Proceedings, eds. W.H. Waller, M.N. Fanelli, J.E. Hollis and A.C. Danks, 408, 403
- Calzetti, D. 2001, *PASP*, 113, 1449
- Calzetti, D., Armus, L., Bohlin, R. C., et al. 2000, *ApJ*, 533, 682
- Calzetti, D., Kennicutt, R. C., Jr., Bianchi, L., et al. 2005, *ApJ*, 633, 871
- Calzetti, D., Kennicutt, R. C., Engelbracht, C. W., et al. 2007, *ApJ*, 666, 870
- Calzetti, D., Wu, S.-Y., Hong, S., et al. 2010, *ApJ*, 714, 1256
- Cardelli, J. A., Clayton, G. C., & Mathis, J. S. 1989, *ApJ*, 345, 245
- Cartledge, S. I. B., Clayton, G. C., Gordon, K. D., et al. 2005, *ApJ*, 630, 355
- Charlot, S., & Fall, S. M. 2000, *ApJ*, 539, 718
- Chhowalla, M., Wang, H., Sano, N., et al. 2003, *Physical Review Letters*, 90, 155504
- Clayton, G. C., Gordon, K. D., & Wolff, M. J. 2000, *ApJS*, 129, 147
- Clayton, G. C., Green, J., Wolff, M. J., et al. 1996, *ApJ*, 460, 313
- Clayton, G. C., Wolff, M. J., Sofia, U. J., Gordon, K. D., & Misselt, K. A. 2003, *ApJ*, 588, 871
- Conroy, C., Schiminovich, D., & Blanton, M. R. 2010, *ApJ*, 718, 184
- Cortese, L., Boselli, A., Franzetti, P., et al. 2008, *MNRAS*, 386, 1157
- Daddi, E., Cimatti, A., Renzini, A., et al. 2004, *ApJ*, 617, 746
- Daddi, E., Dickinson, M., Morrison, G., et al. 2007, *ApJ*, 670, 156
- Dale, D. A., Gil de Paz, A., Gordon, K. D., et al. 2007, *ApJ*, 655, 863
- Dale, D. A., Cohen, S. A., Johnson, L. C., et al. 2009, *ApJ*, 703, 517
- Desert, F.-X., Boulanger, F., & Puget, J. L. 1990, *A&A*, 237, 215
- Duley, W. W. 2006, *ApJ*, 639, L59
- Engelbracht, C. W., Blaylock, M., Su, K. Y. L., et al. 2007, *PASP*, 119, 994
- Fitzpatrick, E. L. 1999, *PASP*, 111, 63
- Fitzpatrick, E. L., & Massa, D. 1986, *ApJ*, 307, 286
- Fitzpatrick, E. L., & Massa, D. 1988, *ApJ*, 328, 734
- Fitzpatrick, E. L., & Massa, D. 1990, *ApJS*, 72, 163
- Fitzpatrick, E. L., & Massa, D. 2007, *ApJ*, 663, 320
- Gadallah, K. A. K., Mutschke, H., & Jaumlger, C. 2011, *A&A*, 528, A56
- Gil de Paz, A., Boissier, S., Madore, B. F., et al. 2007, *ApJS*, 173, 185
- Gordon, K. D., Clayton, G. C., Witt, A. N., & Misselt, K. A. 2000, *ApJ*, 533, 236
- Gordon, K. D., Clayton, G. C., Misselt, K. A., Landolt, A. U., & Wolff, M. J. 2003, *ApJ*, 594, 279
- Gordon, K. D., Misselt, K. A., Witt, A. N., & Clayton, G. C. 2001, *ApJ*, 551, 269
- Granato, G. L., Lacey, C. G., Silva, L., et al. 2000, *ApJ*, 542, 710
- Grasha, K., Calzetti, D., Andrews, J. E., Lee, J. C., & Dale, D. A. 2013, *ApJ*, 773, 174
- Hao, C.-N., Kennicutt, R. C., Johnson, B. D., et al. 2011, *ApJ*, 741, 124
- Hoversten, E. A., Gronwall, C., Vanden Berk, D. E., et al. 2011, *AJ*, 141, 205
- Hutchings, J. B., Bianchi, L., Lamers, H. J. G. L. M., Massey, P., & Morris, S. C. 1992, *ApJ*, 400, L35
- Inoue, A. K., Buat, V., Burgarella, D., et al. 2006, *MNRAS*, 370, 380
- Jiang, P., Ge, J., Zhou, H., Wang, J., & Wang, T. 2011, *ApJ*, 732, 110
- Joblin, C., Leger, A., & Martin, P. 1992, *ApJ*, 393, L79
- Johnson, B. D., Schiminovich, D., Seibert, M., et al. 2007, *ApJS*, 173, 392
- Jogee, S., Scoville, N., & Kenney, J. D. P. 2005, *ApJ*, 630, 837
- Kauffmann, G., Heckman, T. M., White, S. D. M., et al. 2003, *MNRAS*, 341, 33
- Kennicutt, R. C., Jr. 1998, *ARA&A*, 36, 189
- Kennicutt, R. C., Jr., Armus, L., Bendo, G., et al. 2003, *PASP*, 115, 928
- Kennicutt, R. C., Jr., Calzetti, D., Walter, F., et al. 2007, *ApJ*, 671, 333
- Kennicutt, R. C., Jr., Hao, C.-N., Calzetti, D., et al. 2009, *ApJ*, 703, 1672
- Kennicutt, R. C., Jr., Lee, J. C., Funes, S. J., José G., Sakai, S., & Akiyama, S. 2008, *ApJS*, 178, 247
- Kong, X., Charlot, S., Brinchmann, J., & Fall, S. M. 2004, *MNRAS*, 349, 769
- Kong, X., Daddi, E., Arimoto, N., et al. 2006, *ApJ*, 638, 72
- Kong, X., Zhou, X., Chen, J., et al. 2000, *AJ*, 119, 2745
- Kroupa, P. 2002, *Science*, 295, 82
- Leitherer, C., Schaerer, D., Goldader, J. D., et al. 1999, *ApJS*, 123, 3
- Li, A., & Draine, B. T. 2001, *ApJ*, 554, 778
- Lin, L., Zou, H., Kong, X., et al. 2013, *ApJ*, 769, 127
- Lin, W., Zhou, X., Burstein, D., et al. 2003, *AJ*, 126, 1286
- Mallocci, G., Mulas, G., & Joblin, C. 2004, *A&A*, 426, 105
- Mao, Y.-W., Kennicutt, R. C., Jr., Hao, C.-N., Kong, X., & Zhou, X. 2012, *ApJ*, 757, 52
- Martin, D. C., et al. 2005, *ApJ*, 619, L1
- Martin, D. C., Small, T., Schiminovich, D., et al. 2007, *ApJS*, 173, 415
- Meurer, G. R., Heckman, T. M., & Calzetti, D. 1999, *ApJ*, 521, 64
- Misselt, K. A., Clayton, G. C., & Gordon, K. D. 1999, *ApJ*, 515, 128
- Misselt, K. A., Gordon, K. D., Clayton, G. C., & Wolff, M. J. 2001, *ApJ*, 551, 277
- Morrissey, P., Conroy, T., Barlow, T. A., et al. 2007, *ApJS*, 173, 682
- Muñoz-Mateos, J. C., Gil de Paz, A., Boissier, S., et al. 2009, *ApJ*, 701, 1965
- Noll, S., Pierini, D., Cimatti, A., et al. 2009, *A&A*, 499, 69
- Noll, S., Pierini, D., Pannella, M., & Savaglio, S. 2007, *A&A*, 472, 455
- O'Donnell, J. E. 1994, *ApJ*, 422, 158
- Panuzzo, P., Granato, G. L., Buat, V., et al. 2007, *MNRAS*, 375, 640
- Papoular, R. J., & Papoular, R. 2009, *MNRAS*, 394, 2175
- Pérez-González, P. G., et al. 2006, *ApJ*, 648, 987
- Regan, M. W., Thornley, M. D., Bendo, G. J., et al. 2004, *ApJS*, 154, 204
- Relaño, M., Lisenfeld, U., Pérez-González, P. G., Vílchez, J. M., & Battaner, E. 2007, *ApJ*, 667, L141
- Rosa, M. R., & Benvenuti, P. 1994, *A&A*, 291, 1
- Ruiz, A., Bretón, J., & Llorente, J. M. 2005, *Physical Review Letters*, 94, 105501
- Schlegel, D. J., Finkbeiner, D. P., & Davis, M. 1998, *ApJ*, 500, 525
- Seibert, M., et al. 2005, *ApJ*, 619, L55
- Stecher, T. P. 1965, *ApJ*, 142, 1683
- Steglich, M., Bouwman, J., Huisken, F., & Henning, T. 2011, *ApJ*, 742, 2
- Thilker, D. A., et al. 2007, *ApJS*, 173, 572

Vázquez, G. A., & Leitherer, C. 2005, ApJ, 621, 695
 Weingartner, J. C., & Draine, B. T. 2001, ApJ, 548, 296
 Werner, M. W., et al. 2004, ApJS, 154, 1
 Wild, V., Charlot, S., Brinchmann, J., et al. 2011, MNRAS, 417, 1760
 Witt, A. N., & Gordon, K. D. 2000, ApJ, 528, 799
 Xu, C., & Buat, V. 1995, A&A, 293, L65

Zheng, Z., Shang, Z., Su, H., et al. 1999, AJ, 117, 2757
 Zou, H., Zhang, W., Yang, Y., et al. 2011, AJ, 142, 16
 Zubko, V., Dwek, E., & Arendt, R. G. 2004, ApJS, 152, 211

APPENDIX

A

A TEST OF THE FM PARAMETERIZATION IN THE CASE OF VARIOUS DUST-STAR GEOMETRIES

In this paper, we make use of the FM parameterization (Equation (1)) to reproduce attenuation curves considered to have been affected by dust-star geometries. The prescription of Equation (1) is made from the investigation of individual stars where the geometric configuration is simple and can be assumed as dust screens in foreground of stars, whereas in most cases dust and stars are actually mixed together in various forms and the geometric configuration becomes complex. Effective extinction in complex geometries (termed as *attenuation*) is supposed to differ from the extinction imposed by the foreground screen even for the same dust content and the identical grain types, due to the return of scattered light to the sightline of the observer occurring in complex geometries. In this situation, it is necessary to inspect whether the FM parameterization is valid for various dust-star geometries. This appendix presents a simple test to perform this inspection.

We adopt the MW extinction curve as the receptor of geometric effects because of the conspicuous appearance of the three components (i.e., the linear background, the 2175 Angstrom bump, and the FUV rise) in the MW curve; six types of complex dust-star geometries including three global environments (*shell*, *dusty*, and *cloudy*) plus two local distributions (*homogeneous* and *clumpy*), together with the simple configuration of a foreground homogeneous dust screen, are employed in the test. Attenuation curves affected by these geometries are reproduced from the DIRTY radiative transfer model (Gordon et al. 2001; Misselt et al. 2001) and obtained from Witt & Gordon (2000). Definitions of these geometric configurations, i.e., *shell*, *dusty*, *cloudy*, *homogeneous*, and *clumpy*, are addressed in Witt & Gordon (2000).

We fit the obtained attenuation curves with Equation (1). Table 5 presents the coefficients of the FM parameterization for these curves, and Figure 19 shows the modeled data and the best-fitting curves. The data points in Figure 19 are the products of the DIRTY model at $\tau_V = 1.0$; the solid lines are the best-fitting curves for the data points; and the three components of the best-fitting curves are also superimposed, respectively, as the dashed, dotted, and dot-dashed lines.

This figure clearly demonstrates that the combination of the three components prescribed by the FM parameterization is able to successfully reproduce attenuation curves in the case of complex dust-star geometries; all the differences between the attenuation curves with various geometries appear to be the changes in the slope of the linear background, in the strength of the 2175 Angstrom bump, and in the curvature of the FUV rise. This test confirms the validity of the FM parameterization adopted in this paper taking geometric effects into account. For more detailed analyses of the geometric effects, readers are referred to Witt & Gordon (2000); Calzetti (2001).

APPENDIX

B

DISCUSSION WITH THE R_V -DEPENDENT LAW

In addition to the FM parameterization we have employed in this paper, the CCM format of the extinction law provides an alternative description of the extinction curve parameterized only with the total-to-selective extinction R_V , which fits the observations from different sightlines for the Milky Way but lacks the support of substantial evidence from extragalactic sources (Cardelli et al. 1989; Misselt et al. 1999; Clayton et al. 2000; Gordon et al. 2003). In this appendix, we make an additional inspection of this R_V -dependent extinction curve to find out whether or not the galaxies in our sample have this R_V -dependent property in the attenuation curve. Likewise, the CCM law is employed to describe the attenuation features in this work, although it was established by the study of extinction.

Figure 20 shows the variations in IRX and FUV – NUV with the parameter R_V for five constant amounts of $A(V)$ (0.01, 0.1, 0.5, 1.0, and 2.0 mag) charged in accordance with the CCM law. Both IRX and FUV – NUV decrease with increasing R_V , and the declining trends present steeper gradients at higher attenuation. Particularly, FUV – NUV tends to be bluer than intrinsic values when $R_V \gtrsim 3.5$. In actual observations, R_V varies in the approximate range of 2.2–5.8 with a mean value of ~ 3.1 (Fitzpatrick 1999). In Figure 21, we exhibit the CCM curves with $R_V = 2.2, 3.1, \text{ and } 5.8$ in the UV wavelength portion to show the possible variation trend in the CCM curve within the lower and upper limits. When $R_V = 3.1$, the CCM curve is identical in shape to the MW mean curve of the FM parameterization. With increasing R_V , the slope becomes shallower rapidly, and the 2175 Angstrom bump appears to have a slight reduction in strength. These disparities induce more decreases in FUV attenuation than that in NUV attenuation at larger R_V , which therefore explains the trends of IRX and FUV – NUV as a function of R_V in Figure 20.

However, from Figure 22 we can see that the CCM law is inappropriate for characterizing the IRX-UV distributions for the galaxies. And in Figure 23, the CCM law within the range of $2.2 < R_V < 5.8$ fails to interpret the $A(\text{FUV})$ versus $A(\text{FUV}) - A(\text{NUV})$ relations for the galaxies in our sample, and the data points present larger difference between $A(\text{FUV})$ and $A(\text{NUV})$.

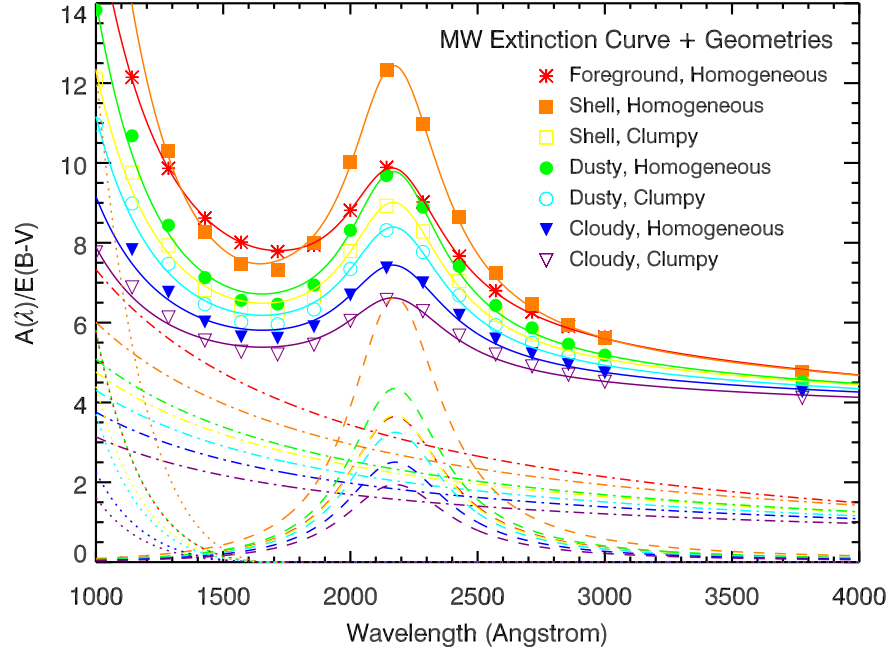


Figure 19. Attenuation curves for the MW extinction mode with different dust-star geometries taken into account. The data points are reproduced with seven dust-star geometries as described by the legend in this figure. The solid lines are the best-fitting curves for the data points; three components of the best-fitting curves are also superimposed, including the 2175 Angstrom bump (dashed lines), the FUV rise (dotted lines), and the linear background (dot-dashed lines). All the lines in this figure are color-coded by the seven dust-star geometries corresponding to the data points. The best-fitting coefficients of the attenuation curves are presented in Table 5.

Table 5
Coefficients of the Attenuation Curves with Different Dust-Star Geometries Taken into Account in Figure 19

Geometry	c_1	c_2	c_3	c_4	γ
Foreground, Homogeneous	-0.461	0.779	3.666	0.446	1.006
Shell, Homogeneous	-0.104	0.611	5.687	0.954	0.858
Shell, Clumpy	0.079	0.468	3.536	0.340	0.961
Dusty, Homogeneous	-0.013	0.510	4.030	0.449	0.926
Dusty, Homogeneous	0.108	0.420	3.260	0.286	1.002
Cloudy, Homogeneous	0.197	0.356	2.722	0.174	1.087
Cloudy, Clumpy	0.245	0.289	2.209	0.125	1.137

at fixed $A(\text{FUV})$ than the model tracks. In the CCM scenario, fitting the data requires $R_V < 2.2$ which would break through the observed lower limit. This discrepancy brings forward a caveat that people should be cautious in applying the CCM law to extragalactic environments. The CCM law formulates the three components in the extinction curve as a function of R_V for our Galaxy, but more studies are required to explore the correlation between the parameters in the attenuation curve and R_V in general cases.

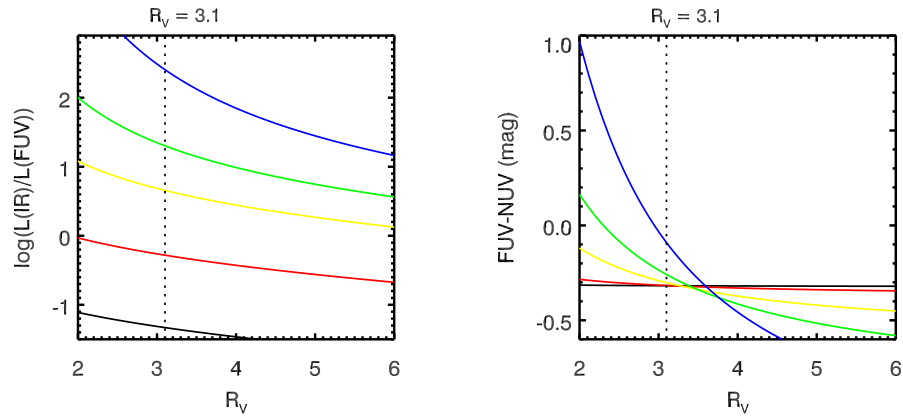


Figure 20. IRX (left) and FUV–NUV (right) vs. R_V reproduced by the CCM extinction law. The solid lines show the correlations modeled by spectral synthesis at fixed amounts of dust extinction: $A(V) = 0.01$ (black), 0.1 (red), 0.5 (yellow), 1.0 (green), and 2.0 (blue); the dotted line marks the position of R_V in each panel.

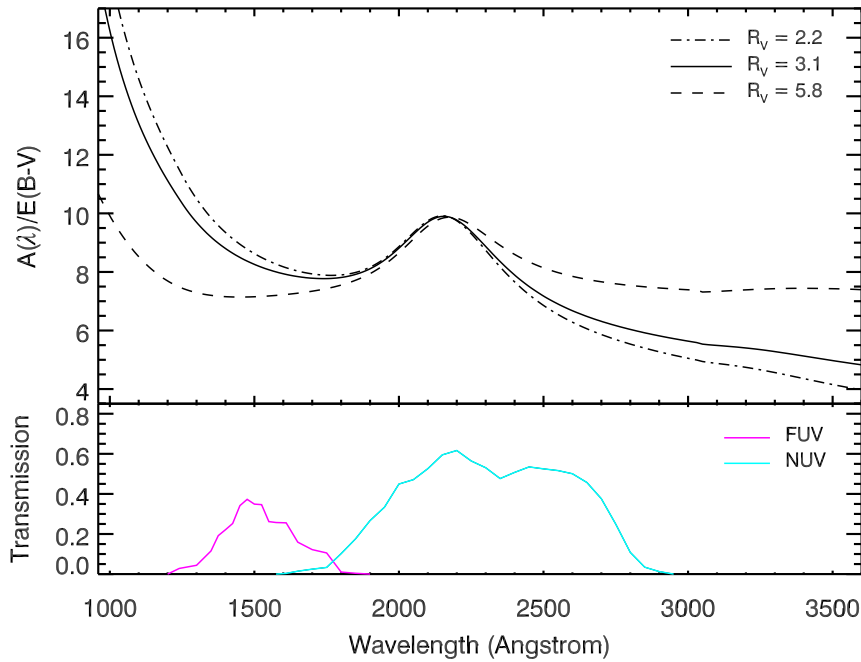


Figure 21. Top: examples of the CCM R_V -dependent extinction curves at the UV wavelength range. The solid line shows the curve in the case of $R_V = 3.1$; the dashed line and the dot-dashed line show the curves in the two cases of $R_V = 5.8$ and $R_V = 2.2$ respectively. Bottom: filter transmission curves of the GALEX FUV (magenta) and NUV (cyan) bands.

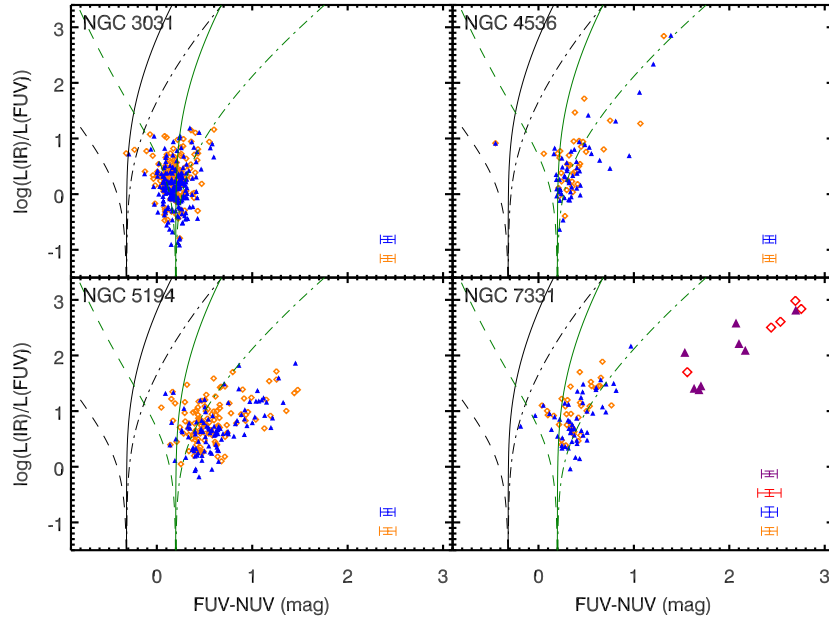


Figure 22. Same diagrams for the UV and the IR clusters inside the galaxies in our sample as plotted in Figure 4, but the lines superimposed on each diagram are reproduced by the CCM extinction curve in the cases of $R_V = 5.8$ (dashed line), $R_V = 3.1$ (solid line), and $R_V = 2.2$ (dot-dashed line) and are color-coded by stellar population age: 2 Myr (black) and 100 Myr (dark green).

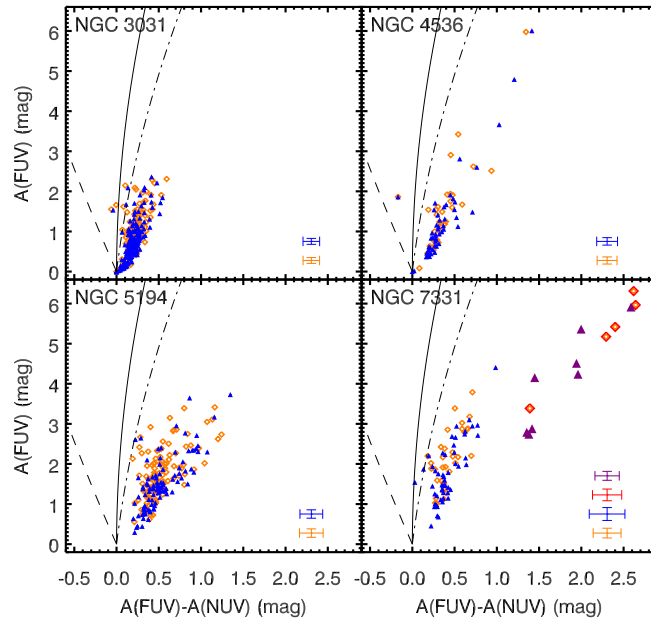


Figure 23. Same diagrams for the UV and the IR clusters inside the galaxies in our sample as plotted in Figure 5, but the lines superimposed on each diagram are reproduced by the CCM extinction curve in the cases of $R_V = 5.8$ (dashed line), $R_V = 3.1$ (solid line), and $R_V = 2.2$ (dot-dashed line).